8-27-2012

FDTD Analysis of Plasmonic and Nanojet Enhanced Photodetectors for Improved Performance

I.M. Mehdi Hasan

I. M. Mehdi Hasan

Candidate

Electrical and Computer Engineering

Department

This thesis is approved, and it is acceptable in quality and form for publication:

Approved by the Thesis Committee:

Payman Zarkesh-Ha, Chairperson

Jamesina J. Simpson, Co-Chairperson

Edward D. Graham, Jr.

Luke F. Lester

FDTD ANALYSIS OF PLASMONIC AND NANOJET ENHANCED PHOTODETECTORS FOR IMPROVED PERFORMANCE

BY

I. M. MEHDI HASAN

BACHELORS
ELECTRICAL ENGINEERING, BANGLADESH UNIVERSITY OF ENGINEERING AND TECHNOLOGY, 2009

THESIS

Submitted in Partial Fulfillment of the
Requirements for the Degree of

Masters of Science
Electrical Engineering

The University of New Mexico
Albuquerque, New Mexico

July, 2012

ACKNOWLEDGEMENTS

I heartily acknowledge Dr. Jamesina Simpson, my advisor and committee co-chair, who believed in me and accepted me as one of her graduate students. She encouraged me throughout my graduate studies and research and provided me with guidance for which I am certainly indebted to her. Her patients, intelligence and assistance have inspired me and I believe, will help me in my future endeavor.

I also thank my committee members, Dr. Payman Zarkesh-Ha, Dr. Edward D. Graham, Jr. and Dr. Luke F. Lester for serving in my committee and for providing recommendations pertaining to this study. I am deeply honored to have such three honorary professors in my committee.

I would also like to thank Cesar Mendes Ruiz, a former student of Dr. Jamesina Simpson for his assistance with FDTD modeling.

Finally, I would like to acknowledge the UNM's Center for Advanced Research Computing (CARC) for providing supercomputing resources under grant number 2007004.

FDTD ANALYSIS OF PLASMONIC AND NANOJET ENHANCED PHOTODETECTORS FOR IMPROVED PERFORMANCE

By

I. M. Mehdi Hasan

B.Sc., Electrical Engineering, Bangladesh University of Engineering and Technology, 2009

M.S., Electrical Engineering, University of New Mexico, 2012

ABSTRACT

The finite-difference time-domain (FDTD) technique is a very flexible and robust means to solve problems spanning a broad range of applications (defense, communication, computing, semiconductor devices and biomedicine), especially where geometrical complexities, nonlinearities and multiphysics dominate. In this thesis, novel photodetectors are developed via FDTD having sub-wavelength active areas that yield enhanced optical absorption at near-infrared (NIR) wavelengths by way of plasmonics or photonic nanojets.

The response time of photodiodes is primarily limited by two factors: (1) the transit time of photo-generated carriers to the electrode and (2) depletion layer capacitance of the semiconductor. The former requires a thinner depletion layer, resulting in a large depletion layer capacitance. To suppress the increase of the depletion layer capacitance, it

is necessary to decrease the active area of the photodiode with depletion layer thickness. However, the smaller the active area the lower the output of the photodiode under the constant optical power density. To overcome the trade-off between speed and responsivity, the incident light should be efficiently confined within a small active area. Surface plasmons play an important role in this phenomenon as surface plasmons can enhance the near-field when excited by a certain wavelength. Resonant surface plasmons can confine strong optical near fields in a sub wavelength volume, this has been demonstrated for near- infrared dipole antennas.

As an alternative to plasmonics it is proposed here that photonic nanojets may be employed to focus light onto the small active region of a photodetector. A photonic nanojet is a narrow, high-intensity electromagnetic beam that propagates into the background medium from the shadow side surface of a plane-wave illuminated loss-less dielectric micro-cylinder or micro-sphere of diameter greater than the illuminating wavelength, λ. The transverse beam width of the nanojet can be as small as $\lambda/3$ and length can be as long as 20λ, so we can use a photonic nanojet to concentrate the energy into a small region. By using the E-field enhancement in a sub-wavelength active area provided by the photonic nanojet and comparing it with the enhancement of the plasmonic structures, we may improve the responsivity and speed of the photodetector.

Table of Contents

List of Figures

Chapter 1

Introduction

1.1 Modeling Overview

The finite-difference time-domain (FDTD) technique [1] is a very flexible and robust means to solve problems spanning a broad range of applications (defense, communication, computing, semiconductor devices and biomedicine), especially where geometrical complexities, nonlinearities and multiphysics dominate. In this thesis, novel photodetectors are developed via FDTD having sub-wavelength active areas that yield enhanced optical absorption at near-infrared wavelengths by way of plasmonics or photonic nanojets. For FDTD modeling we use Yee algorithm and we begin using Maxwell's curl equations in 3D for non dispersive material ($\vec{J}$ and σ are zero), and for dispersive material ($\vec{J}$ and σ are non-zero) we considered no magnetic source or magnetic loss. Ampere's law FDTD updates for non dispersive material (in this case Lorentz-Drude Medium) is: $\nabla X \vec{H} = \varepsilon_0 \frac{\delta \vec{E}}{\delta t} + \sigma \vec{E} + \vec{J}_{tot}$ and for non dispersive material is: $\nabla X \vec{H} = \varepsilon_0 \frac{\delta \vec{E}}{\delta t}$ [1]. Where, $\vec{E}$: electric field (volts / meter), $\vec{H}$: magnetic field (amperes / meter), ε_0 : free-space permittivity (8.854×10^{-12} farads / meter), $\vec{J}$ = $\vec{J}_{tot}$: polarization current due to Drude and Lorentz poles (volts / meter^2) and σ : electric conductivity (siemens / meter). For modeling our dispersive medium, we use Lorentz-Drude medium, as it is often used for parameterization of the optical

constants of metals [2, 3]. In this thesis, a plane wave is employed that is x-polarized and is generated using total-field scattered-field technique (TFSF). TFSF technique is used since the generated plane wave can have an arbitrary and easily specified propagation direction, polarization and a planar wavefront that is perpendicular to the direction of propagation [1]. As our computational domain is extensive, a parallel version of the FDTD algorithm is implemented that can operate in multi-processor computers or computer clusters. The computational domain is divided into sub-domains and the tangential field components of the domains are passed between the adjacent interfaces at each time step with an appropriate synchronization procedure, which is provided by the message passing interface (MPI) library. For our absorbing boundary conditions (ABC), we used convolutional perfectly matched layer (CPML), as the CPML accommodates more general metric tensor coefficients that can lead to improved absorption of slowly varying evanescent waves [1].

1.2 Plasmonic and Nanojet Enhancement

The response time of photodiodes is primarily limited by two factors: (1) the transit time of photo-generated carriers to the electrode and (2) the depletion layer capacitance of the semiconductor. The former requires a thinner depletion layer, resulting in a large depletion layer capacitance. To suppress the increase of the depletion layer capacitance, it is necessary to decrease the active area of the photodiode with the depletion layer thickness. However, the smaller the active area the lower the output of the photodiode under the constant optical power density. To overcome the trade-off between speed and responsivity, the incident light should be efficiently confined within a small active area

[4]. Optical near-field localized around the nanometric element has the potential to satisfying such a requirement for the photodiode. If we can use a localized interaction between optical near-field and a small semiconductor element, a high-speed response and a sufficient responsivity may be possible.

Surface plasmons play an important role in this phenomenon. Surface plasmons can enhance the near-field when excited by a certain wavelength. It has recently been demonstrated that photo-generation of carriers in silicon can be enhanced by a surface-plasmon antenna at a wavelength of 840nm for a grating structure, but this antenna occupies a large area [5, 6, 7]. Resonant surface plasmons lead to a large enhancement of optical near-field in a sub-wavelength volume, which has been demonstrated for dipole and bow-tie antenna structures at visible wavelengths [5].

The photonic nanojet is a narrow, high-intensity electromagnetic beam that propagates into the background medium from the shadow side surface of a plane-wave illuminated loss-less dielectric micro-cylinder or micro-sphere of diameter greater than the illuminating wavelength, λ. Photonic nanojets with certain diameter has a spectrum over a certain range of wavelength depending upon the diameter of the sphere. The transverse beam-width of the nanojet can be as small as $\lambda/3$ and the longitudinal length can be as long as 20λ, so it can be used to concentrate energy in a small surface area and by adjusting the distance of the sphere, we can model our device for a small area of E-field confinement considering the thickness [8]. In this way, we can model a photodetector with high responsivity as well as high speed.

Chapter 2

FDTD Modeling

2.1 Introduction of FDTD

FDTD is a grid-based, wide-band computational technique for solving the full-wave Maxwell's equations [1].

Maxwell's curl equations in 3D and the six corresponding coupled scalar equations are given below:

Faraday's law:

$$\nabla X \vec{E} = -\mu \frac{\delta \vec{H}}{\delta t} - \vec{M}$$

Ampere's law:

$$\nabla X \vec{H} = \varepsilon \frac{\delta \vec{E}}{\delta t} + \vec{J}$$

And $\varepsilon = \varepsilon_r \varepsilon_0$

Where, ε : electrical permittivity (farads / meter),

ε_r : relative permittivity (dimensionless scalar).

$\vec{J}$ and $\vec{M}$ can act as independent sources of $\vec{E}$ and $\vec{H}$ field energy, $J_{source}^{\rightarrow}$ and $M_{source}^{\rightarrow}$. If we allow for materials with isotropic, nondispersive electric and magnetic losses that attenuate $\vec{E}$ -and $\vec{H}$ -fields via conversion to heat energy. This yields

$$\vec{J} = J_{source}^{\rightarrow} + \sigma \vec{E} \quad ; \quad \vec{M} = M_{source}^{\rightarrow} + \sigma^{M} \vec{H}$$

Where,

σ^M: equivalent magnetic loss (ohms / meter)

This yields Maxwell's curl equations in linear, isotropic, nondispersive, lossy materials:

$$\frac{\delta \vec{H}}{\delta t} = \frac{-1}{\mu} \nabla X \vec{E} - \frac{1}{\mu}(\vec{M_{source}} + \sigma^{M} \vec{H})$$

$$\frac{\delta \vec{E}}{\delta t} = \frac{1}{\varepsilon} \nabla X \vec{H} - \frac{1}{\varepsilon}(\vec{J_{source}} + \sigma \vec{E})$$

This yields the following system of six coupled scalar equations:

$$\frac{\delta H_x}{\delta t} = \frac{1}{\mu}[\frac{\delta E_y}{\delta z} - \frac{\delta E_z}{\delta y} - (M_{source_x} + \sigma^{M} H_x)] \quad \text{.....(1a)}$$

$$\frac{\delta H_y}{\delta t} = \frac{1}{\mu}[\frac{\delta E_z}{\delta x} - \frac{\delta E_x}{\delta z} - (M_{source_y} + \sigma^{M} H_y)] \quad \text{.....(1b)}$$

$$\frac{\delta H_z}{\delta t} = \frac{1}{\mu}[\frac{\delta E_x}{\delta y} - \frac{\delta E_y}{\delta x} - (M_{source_z} + \sigma^{M} H_z)] \quad \text{.....(1c)}$$

$$\frac{\delta E_x}{\delta t} = \frac{1}{\varepsilon}[\frac{\delta H_z}{\delta y} - \frac{\delta H_y}{\delta z} - (J_{source_x} + \sigma E_x)] \quad \text{.....(2a)}$$

$$\frac{\delta E_y}{\delta t} = \frac{1}{\varepsilon}[\frac{\delta H_x}{\delta z} - \frac{\delta H_z}{\delta x} - (J_{source_y} + \sigma E_y)] \quad \text{.....(2b)}$$

$$\frac{\delta E_z}{\delta t} = \frac{1}{\varepsilon}[\frac{\delta H_y}{\delta x} - \frac{\delta H_x}{\delta y} - (J_{source_z} + \sigma E_z)] \quad \text{.....(2c)}$$

2.2 The Yee Algorithm [1]

In 1966 Yee originated a set of finite-difference equations for the time-dependent Maxwell's curl equations. Yee algorithm centers its $\vec{E}$ and $\vec{H}$ components in three-dimensional space so that every $\vec{E}$ component is surrounded by four circulating $\vec{H}$ components, and every $\vec{H}$ component is surrounded by four circulating $\vec{E}$ components.

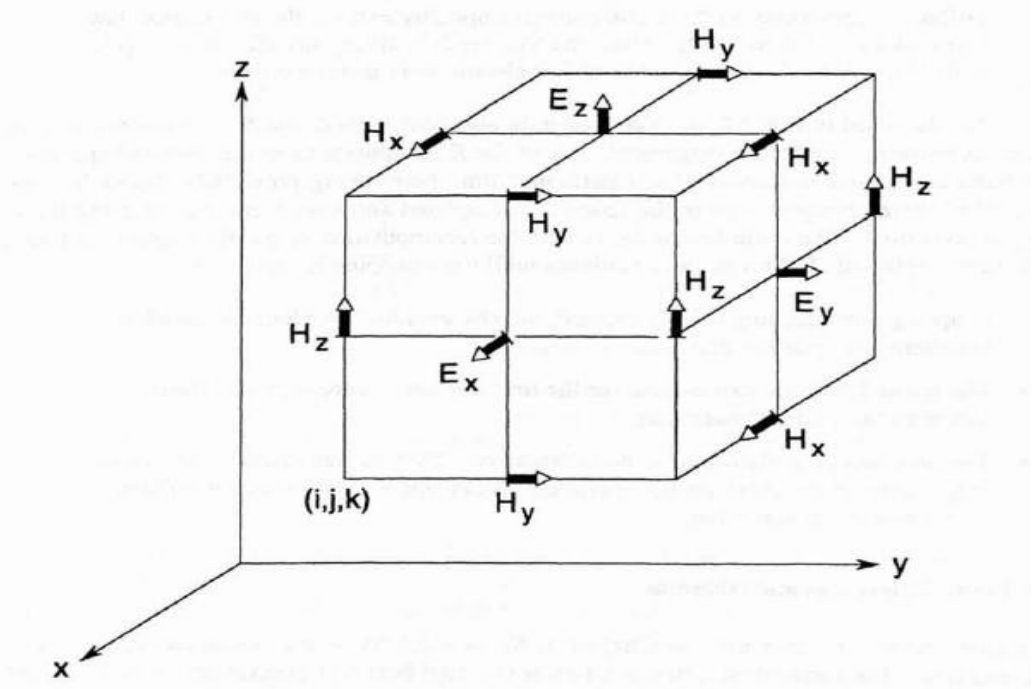

Figure 1: Position of the electric and magnetic field vector components about a cubic unit cell of the Yee space lattice (figure courtesy of [1]).

Yee algorithm also centers its $\vec{E}$ and $\vec{H}$ components in time, in what is termed a leapfrog arrangement.

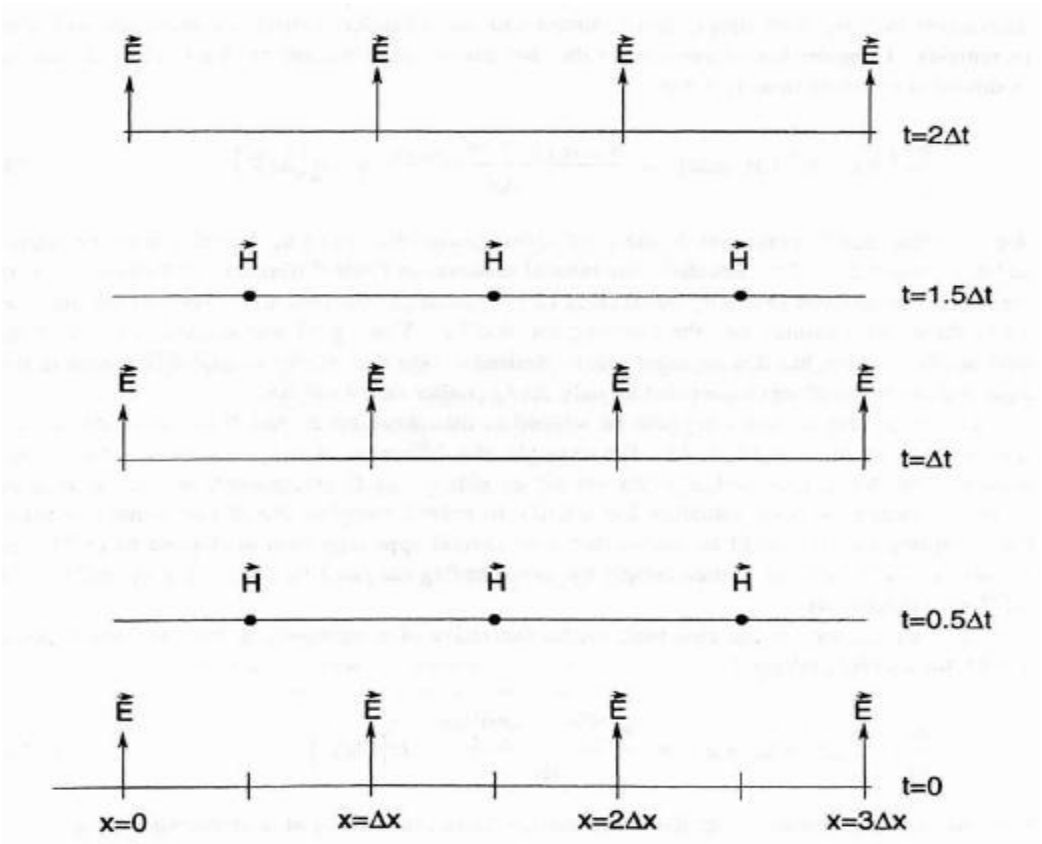

Figure 2: Time- discretization scheme. Space-time chart of the Yee algorithm for a one-dimensional wave propagation example showing the use of central differences for the space derivatives and leapfrog for the time derivatives (figure courtesy of [1]).

We denote any function u of space and time evaluated at a discrete point in the grid and at a discrete point in time as:

$$u(i\Delta x, j\Delta y, k\Delta z, n\Delta t) = u^{n}_{i,j,k}$$

Where Δt is the time increment, assumed uniform over the observation interval, Δx, Δy and Δz are, respectively, the lattice space increments in the x, y and z coordinate directions and i, j, k, n are integers.

Yee used centered finite-difference (central-difference) expressions for the space and time derivatives that are both simply programmed and second-order accurate in the space and time increments. The first partial space derivative of u in x-direction:

$$\frac{\delta u}{\delta x}(i\Delta x, j\Delta y, k\Delta z, n\Delta t)=\frac{u^{n}_{i+1/2,j,k}-u^{n}_{i-1/2,j,k}}{\Delta x}+O[(\Delta x)^2]$$

We note the ±1/2 increment in the i subscript of u, denoting a space finite-difference over ±1/2 Δx.

Similarly,

$$\frac{\delta u}{\delta t}(i\Delta x, j\Delta y, k\Delta z, n\Delta t)=\frac{u^{n+1/2}_{i,j,k}-u^{n-1/2}_{i,j,k}}{\Delta t}+O[(\Delta t)^2]$$

Now the ±1/2 increment is in the n superscript of u, denoting time finite-difference over ±1/2 Δt.

Now we apply the above ideas and notation to achieve a numerical approximation of the Maxwell's curl equations in 3D given by equations (1) and (2). For example:

$$\frac{\delta E_x}{\delta t}=\frac{1}{\varepsilon}\left[\frac{\delta H_z}{\delta y}-\frac{\delta H_y}{\delta z}-(J_{source_x}+\sigma E_x)\right]$$

Can be expressed as:

$$\frac{E^{n+1/2}_{x\,i,j+1/2,k+1/2}-E^{n-1/2}_{x\,i,j+1/2,k+1/2}}{\Delta t}=\left(\frac{H^{n}_{z\,i,j+1,k+1/2}-H^{n}_{z\,i,j,k+1}}{\Delta y}-\frac{H^{n}_{y\,i,j+1/2,k+1}-H^{n}_{y\,i,j+1/2,k}}{\Delta z}\right)$$
$$\left(-J^{n}_{x\,i,j+1/2,k+1/2}-\sigma_{i,j+1/2,k+1/2}E^{n}_{x\,i,j+1/2,k+1/2}\right)\left(\frac{1}{\varepsilon_{i,j+1/2,k+1/2}}\right).....(3)$$

Using semi-implicit approximation:

$$E_{x}^{n}{}_{i,j+1/2,k+1/2}=\frac{E_{x}^{n+1/2}{}_{i,j,k}+E_{x}^{n-1/2}{}_{i,j,k}}{2}$$

We get from equation (3),

$$E_{x}^{n+1/2}{}_{i,j+1/2,k+1/2}=\left[\frac{1-\frac{\sigma_{i,j+1/2,k+1/2}\Delta t}{2\varepsilon_{i,j+1/2,k+1/2}}}{1+\frac{\sigma_{i,j+1/2,k+1/2}\Delta t}{2\varepsilon_{i,j+1/2,k+1/2}}}\right]E_{x}^{n-1/2}{}_{i,j+1/2,k+1/2}$$

$$+\left[\frac{\frac{\Delta t}{\varepsilon_{i,j+1/2,k+1/2}}}{1+\frac{\sigma_{i,j+1/2,k+1/2}\Delta t}{2\varepsilon_{i,j+1/2,k+1/2}}}\right]\left[\frac{H_{z}^{n}{}_{i,j+1,k+1/2}-H_{z}^{n}{}_{i,j,k+1/2}}{\Delta y}-\frac{H_{y}^{n}{}_{i,j+1/2,k+1}-H_{y}^{n}{}_{i,j+1/2,k}}{\Delta z}-J_{x}^{n}{}_{i,j+1/2,k+1/2}\right]$$

This can be written as:

$$E_{x}^{n+1/2}{}_{i,j+1/2,k+1/2}=Ca_{x}{}_{i,j+1/2,k+1/2}E_{x}^{n-1/2}{}_{i,j+1/2,k+1/2}$$
$$+Cb_{x}{}_{i,j+1/2,k+1/2}\left[H_{z}^{n}{}_{i,j+1,k+1/2}-H_{z}^{n}{}_{i,j,k+1/2}+H_{y}^{n}{}_{i,j+1/2,k}-H_{y}^{n}{}_{i,j+1/2,k+1}-J_{x}^{n}{}_{i,j+1/2,k+1/2}\Delta\right].....(4)$$

Where,

$$Ca_{x}{}_{i,j,k}=\frac{\left(1-\frac{\sigma_{i,j,k}\Delta t}{2\varepsilon_{i,j,k}}\right)}{\left(1+\frac{\sigma_{i,j,k}\Delta t}{2\varepsilon_{i,j,k}}\right)} \quad \text{and}$$

$$Cb_{x}{}_{i,j,k}=\frac{\left(\frac{\Delta t}{\varepsilon_{i,j,k}\Delta}\right)}{\left(1+\frac{\sigma_{i,j,k}\Delta t}{2\varepsilon_{i,j,k}}\right)} \quad \text{and } \Delta x = \Delta y = \Delta z = \Delta$$

Similarly,

$$\frac{\delta H_x}{\delta t}=\frac{1}{\mu}\left[\frac{\delta E_y}{\delta z}-\frac{\delta E_z}{\delta y}-\left(M_{source_x}+\sigma^M H_x\right)\right]$$

$$H_{x}^{n+1}{}_{i-1/2,j+1,k+1}=Da_{x}{}_{i-1/2,j+1,k+1}H_{x}^{n}{}_{i-1/2,j+1,k+1}$$
$$+Db_{x}{}_{i-1/2,j+1,k+1}\left[E_{y}^{n+1/2}{}_{i-1/2,j+1,k+3/2}-E_{y}^{n+1/2}{}_{i-1/2,j+1,k+1/2}+E_{z}^{n+1/2}{}_{i-1/2,j+1/2,k+1}-E_{z}^{n+1/2}{}_{i-1/2,j+3/2,k+1}\right].....(5)$$

Where,

$$Da_{x}{}_{i,j,k}=1$$

$$Db_{x}{}_{i,j,k}=\left(\frac{\Delta t}{\mu_{i,j,k}\Delta}\right) \quad \text{and } \Delta x = \Delta y = \Delta z = \Delta$$

And considering no magnetic source or $\vec{M}=0$ and no magnetic loss, $\sigma^M=0$.

Chapter 3

Dispersive Materials

3.1 Linear Dispersive Materials

Current and emerging technological applications in bioelectromagnetics, biophotonics, nanophotonics, and high-power microwaves involve electromagnetic wave interactions at the wavelength or subwavelength scale with materials having frequency-dispersive dielectric properties. If a material's permittivity and / or permeability vary with frequency at low intensities of the wave's E- and H-fields, it is known as linear dispersive material [1]. For example, in this thesis, we use nano-meter scale antenna are made of gold, which is a linear dispersive material. In this thesis, the time-domain auxiliary differential equations (ADE) for implementing FDTD models of dispersive materials linking the polarization and the electric flux density is employed. And the Lorentz-Drude model is used for parameterization of the optical constants of metals [2, 3].

3.2 Lorentz-Drude Model

The relative permittivity of Lorentz-Drude medium in the frequency domain can be expressed as following:

$$\varepsilon_r(\omega) = \varepsilon_r^{(f)}(\omega) + \varepsilon_r^{(b)}(\omega)$$

This separates explicitly the free electron effects (Drude model) from bound electron effects (Lorentz Model).

The free electron effects or the Drude model is given by:

$$\varepsilon_r^{(f)}(\omega)=1-\frac{\Omega_p^2}{\omega(\omega-i\Gamma_0)}$$

The bound electron effects or the Lorentz model is given by:

$$\varepsilon_r^{(b)}(\omega)=\sum_{j=1}^{k}\frac{f_j\omega_p^2}{(\omega_j^2-\omega^2)+i\omega\Gamma_j}$$

Where, ω_p is the plasma frequency, k is the number of oscillators with frequency ω_j, strength f_j, and lifetime $1/\Gamma_j$, while $\Omega_p=\sqrt{f_0}\omega_p$ is the plasma frequency associated with the free electron transitions with oscillator strength f_0 and damping constant Γ_0.

3.3 Formulation for Multiple Lorentz-Drude Poles

At any particular $\vec{E}$ observation point, Ampere's law in the time domain can be expressed for Lorentz-Drude medium as,

$$\nabla X\vec{H}=\varepsilon_0\frac{\delta\vec{E}}{\delta t}+\sigma\vec{E}+\vec{J}_{tot}.....(6)$$

and

$$\vec{J}_{tot}=\underset{f}{\vec{J}}+\underset{b}{\vec{J}}$$

where,

$\underset{f}{\vec{J}}$ is the polarization current associated with Drude pole.

$\underset{b}{\vec{J}}$ is the polarization current associated with Lorentz poles.

3.3.1 Drude Model

A phasor polarization current associated with Drude pole in frequency domain is given by:

$$\hat{J}_f = -\varepsilon_0 \Omega_p^2 \frac{(i\omega)}{\omega(\omega - i\Gamma_0)} \hat{E}$$

This gives,

$$\omega^2 \hat{J}_f - i\omega\Gamma_0 \hat{J}_f = -i\omega\varepsilon_0 \Omega_p^2 \hat{E}$$

Taking the inverse Fourier Transformation,

$$\frac{\delta^2 J_f}{\delta t^2} + \Gamma_0 \frac{\delta J_f}{\delta t} = \varepsilon_0 \Omega_p^2 \frac{\delta E}{\delta t}$$

Now applying central differences for time, we get,

$$\frac{J_f^{n+1} - 2J_f^n + J_f^{n-1}}{\Delta t^2} + \Gamma_0 \frac{J_f^{n+1} - J_f^{n-1}}{2\Delta t} = \varepsilon_0 \Omega_p^2 \frac{E^{n+1} - E^{n-1}}{2\Delta t}$$

This can be written as,

$$J_f^{n+1} = \gamma_f J_f^n + \kappa_f J_f^{n-1} + \beta_f \left[\frac{E^{n+1} - E^{n-1}}{2\Delta t}\right]$$

where,

$$\gamma_f = \frac{2}{1 + \Delta t \frac{\Gamma_0}{2}}$$

$$\kappa_f = \frac{\Delta t \frac{\Gamma_0}{2} - 1}{\Delta t \frac{\Gamma_0}{2} + 1} \quad \text{And} \quad \beta_f = \frac{\varepsilon_0 \Omega_p^2 \Delta t^2}{1 + \Delta t \frac{\Gamma_0}{2}}$$

Now,

$$J_f^{n+1/2} = \frac{1}{2}(J_f^n + J_f^{n+1})$$

$$\Rightarrow$$

$$J_f^{n+1/2} = \frac{1}{2}[(1+\gamma_f) J_f^n + \kappa_f J_f^{n-1} + \beta_f (\frac{E^{n+1} - E^{n-1}}{2\Delta t})] \ldots\ldots\ldots\ldots\ldots (7)$$

3.3.2 Lorentz Model

A phasor polarization current associated with Lorentz pole in frequency domain is given by:

$$\hat{J}_b = \varepsilon_0 f_j \omega_p^2 \frac{(i\omega)}{\omega_j^2 + i\omega\Gamma_j - \omega^2} \hat{E}$$

This gives,

$$\omega_j^2 \hat{J}_b + i\omega\Gamma_j \hat{J}_b - \omega^2 \hat{J}_b = i\omega\varepsilon_0 f_j \omega_p^2 \hat{E}$$

Taking the inverse Fourier transformation:

$$\frac{\delta^2 J_b}{\delta t^2} + \Gamma_j \frac{\delta J_b}{\delta t} + \omega_j^2 J_b = \varepsilon_0 f_j \omega_p^2 \frac{\delta E}{\delta t}$$

Now applying central differences for time, we get,

$$\frac{J_b^{n+1} - 2J_b^n + J_b^{n-1}}{\Delta t^2} + \Gamma_j \frac{J_b^{n+1} - J_b^{n-1}}{2\Delta t} + \omega_j^2 J_b = \varepsilon_0 f_j \omega_p^2 (\frac{E^{n+1} - E^{n-1}}{2\Delta t})$$

This can be written as,

$$J_b^{n+1} = \alpha_b J_b^n + \xi_b J_b^{n-1} + \gamma_b \left[\frac{E^{n+1} - E^{n-1}}{2\Delta t} \right]$$

where,

$$\alpha_b = \frac{2 - \omega_j^2 (\Delta t)^2}{1 + \Delta t \frac{\Gamma_0}{2}}$$

$$\xi_b = \frac{\Delta t \frac{\Gamma_j}{2} - 1}{\Delta t \frac{\Gamma_j}{2} + 1} \quad \text{and} \quad \gamma_b = \frac{\varepsilon_0 f_j \omega_p^2 \Delta t^2}{1 + \Delta t \frac{\Gamma_j}{2}}$$

Now,

$$J_b^{n+1/2} = \frac{1}{2} (J_b^n + J_b^{n+1})$$

$$\Rightarrow \quad J_b^{n+1/2} = \frac{1}{2} \left[(1 + \alpha_b) J_b^n + \xi_b J_b^{n-1} + \gamma_b \left(\frac{E^{n+1} - E^{n-1}}{2\Delta t} \right) \right] \ldots\ldots\ldots\ldots\ldots\ldots (8)$$

As,

$$\vec{J}_{tot} = \vec{J}_f + \vec{J}_b$$

Hence,

$J_{tot}^{n+1/2} = (J_f^{n+1/2} + \sum_{b=1}^{5} J_b^{n+1/2})$, as there are 1 pole in the Drude model and 5 poles in the Lorentz model, such that f=1 and b varies from 1 to 5.

Now from equation (4):

$$\nabla X H^{n+1/2} = \varepsilon_0 \left(\frac{E^{n+1} - E^n}{\Delta t} \right) + \sigma \left(\frac{E^{n+1} + E^n}{2} \right) + J_f^{n+1/2} + \sum_{b=1}^{5} J_b^{n+1/2} \ldots\ldots\ldots\ldots\ldots\ldots (9)$$

Using the value of $J_f^{n+1/2}$ and $J_b^{n+1/2}$ from equation (7) and (8) in equation (9) and rearranging, we get,

$$E^{n+1}=C_1E^{n-1}+C_2E^n+C_3[\nabla X H^{n+1/2}-\frac{1}{2}[\sum_{b=1}^{5}((1+\alpha_b)J_b^n+\xi_b J_b^{n-1})+(1+\gamma_f)J_f^n+\kappa_f J_f^{n-1}]]$$

where,

$$C_1=\frac{\frac{1}{2}[\sum_{b=1}^{5}\gamma_b+\beta_f]}{2\varepsilon_0+\Delta t\sigma+\frac{1}{2}[\sum_{b=1}^{5}\gamma_b+\beta_f]}$$

$$C_2=\frac{2\varepsilon_0-\Delta t\sigma}{2\varepsilon_0+\Delta t\sigma+\frac{1}{2}[\sum_{b=1}^{5}\gamma_b+\beta_f]} \quad \text{and} \quad C_3=\frac{2\Delta t}{2\varepsilon_0+\Delta t\sigma+\frac{1}{2}[\sum_{b=1}^{5}\gamma_b+\beta_f]}$$

Values of all the optical constants were taken from [2].

Chapter 4

The Total-Field / Scattered-Field Technique

4.1 Introduction of TFSF

The total-field / scattered-field (TFSF) formulation realizes a plane-wave source that avoids the difficulties caused by using either hard sources or the initial condition approach [1]. The TFSF formulation is based on the linearity of Maxwell's equations. It assumes that the physical total electric and magnetic fields $\vec{E_{total}}$ and $\vec{H_{total}}$ can be decomposed as follows:

$$\vec{E_{total}} = \vec{E_{inc}} + \vec{E_{scat}} \qquad \vec{H_{total}} = \vec{H_{inc}} + \vec{H_{scat}}$$

Here, $\vec{E_{inc}}$ and $\vec{H_{inc}}$ are the values of the incident fields, assumed to be known at all points of the space lattice at all time-steps. $\vec{E_{scat}}$ and $\vec{H_{scat}}$ are the values of the scattered fields, which are initially unknown. These results are from the interaction of the incident wave with any material in the space lattice. The Yee algorithm can be applied with equal validity to the incident field, scattered field and total field, which allows zoning of the space lattice into two distinct regions as shown in Figure 3. For Region 1, the total fields are assumed to be stored in the computer memory while in Region 2, the scattered fields are assumed to be stored in the computer memory.

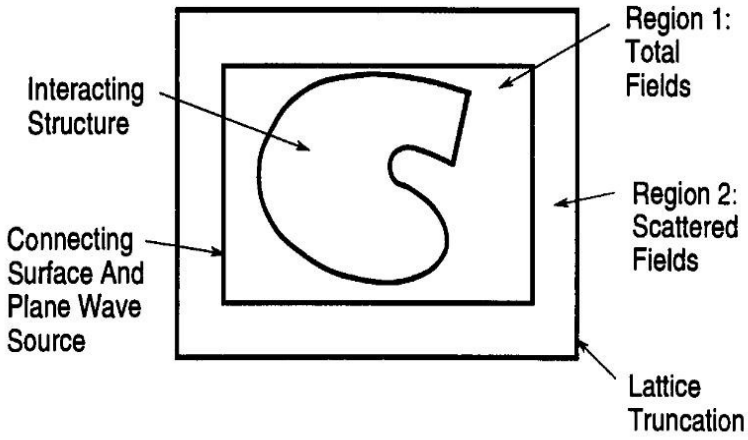

Figure 3: Total-field and scattered-field regions, connecting virtual surface (plane-wave source) and lattice truncation (absorbing boundary condition) in 2D (figure courtesy of [1]).

The incident plane wave generated using TF/SF technique meets the following challenges:

- An arbitrary and easily specified propagation direction, polarization, time waveform and duration;
- A planar wavefront that is perpendicular to the direction of propagation;
- A constant amplitude along any plane parallel to the wavefront [1].

4.2 3D Formulation of TFSF Technique

In three dimensions, the interface surface of the total-field and scattered-field regions in the Yee space lattice is composed of six flat planes forming a closed rectangular box shown in the following figure:

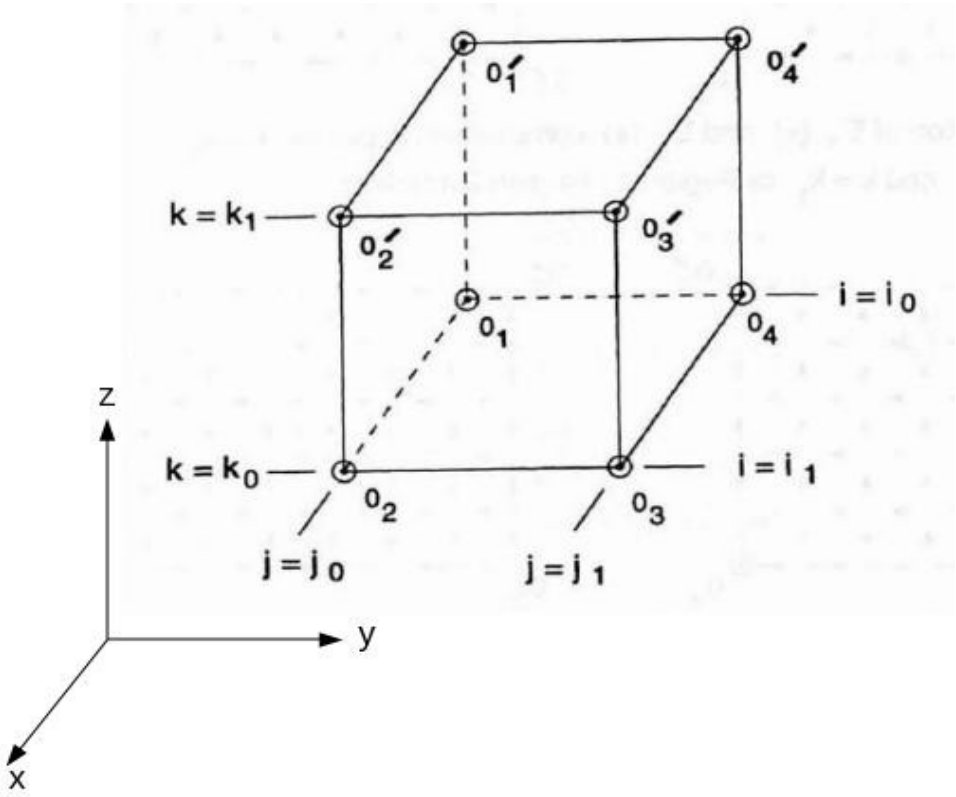

Figure 4: Six-sided total-field/scattered-field interface surface for 3D FDTD space lattice and coordinate origins for calculation of incident field (figure courtesy of [1]).

Each box face contains two tangential $\vec{E}$ components [1] and as in this thesis our incident plane wave is x-polarized and propagating in the z direction hence, our considered plane contains E_x and E_z. Our incident wave for TFSF technique is one dimensional as it simplifies our calculations, which has only $\vec{E_{x,inc}}$ and $\vec{H_{y,inc}}$ propagating in the z direction.

Figure of our considered plane is given below:

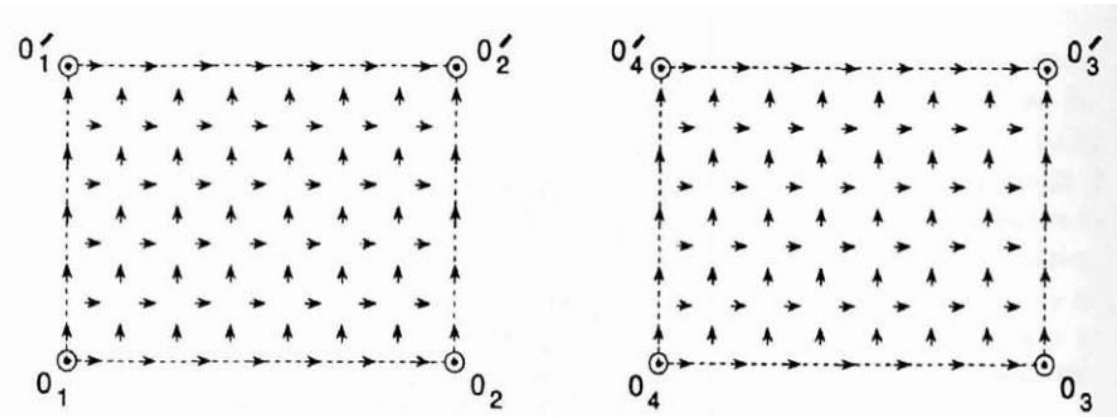

Figure 5: Location of E_x (→) and E_z (↑) components in planes $j=j_0$ and $j=j_1$ of Region-1 and Region-2 interface (figure courtesy of [1]).

4.3 Consistency Conditions

In analogy to the 2D consistency conditions, the consistency conditions for the $\vec{E}$ components in our considered face are given by:

$k=k_0$ Face: E_x ($i=i_0+1/2,.....,i_1-1/2$; $j=j_0,.....,j_1$; $k=k_0$)

$$E_{x}^{n+1}{}_{i,j,k_0} = [E_{x}^{n+1}{}_{i,j,k_0}]_{update\ as\ Eqn(4)} + \frac{\Delta t}{\varepsilon_0 \Delta} H_{y,inc}^{\ n+1/2}{}_{k_0-1/2}$$

$k=k_1$ Face: E_x ($i=i_0+1/2,.....,i_1-1/2$; $j=j_0,.....,j_1$; $k=k_1$)

$$E_{x}^{n+1}{}_{i,j,k_1} = [E_{x}^{n+1}{}_{i,j,k_1}]_{update\ as\ Eqn(4)} - \frac{\Delta t}{\varepsilon_0 \Delta} H_{y,inc}^{\ n+1/2}{}_{k_1+1/2}$$

$i=i_0$ Face: E_z ($i=i_0$; $j=j_0,.....,j_1$; $k=k_0+1/2,.....,k_1-1/2$)

$$E_{z}^{n+1}{}_{i_0,j,k} = [E_{z}^{n+1}{}_{i_0,j,k}]_{update\ as\ Eqn(4)} - \frac{\Delta t}{\varepsilon_0 \Delta} H_{y,inc}^{\ n+1/2}{}_{i_0-1/2}$$

$i=i_1$ Face: E_z ($i=i_1$; $j=j_0$,.....,j_1; $k=k_0+1/2$,.....,$k_1-1/2$)

$$E_{z}^{n+1}{}_{i_1,j,k}=\left[E_{z}^{n+1}{}_{i_1,j,k}\right]_{update\ as\ Eqn(4)}+\frac{\Delta t}{\varepsilon_0\Delta}H_{y,inc}^{\ n+1/2}{}_{i_1+1/2}$$

The consistency conditions for $\vec{H}$ components located 0.5Δ outside of each face of the TFSF interface in three dimensions are given by,

$j=j_0-1/2$ Face: H_z ($i=i_0+1/2$,.....,$i_1-1/2$; $j=j_0-1/2$; $k=k_0$,.....,k_1)

$$H_{z}^{n+1/2}{}_{i,j_0-1/2,k}=\left[H_{z}^{n+1/2}{}_{i,j_0-1/2,k}\right]_{update\ as\ Eqn(5)}-\frac{\Delta t}{\mu_0\Delta}E_{x,inc}^{\ n}{}_{j_0}$$

$j=j_1+1/2$ Face: H_z ($i=i_0+1/2$,.....,$i_1-1/2$; $j=j_1+1/2$; $k=k_0$,.....,k_1)

$$H_{z}^{n+1/2}{}_{i,j_1+1/2,k}=\left[H_{z}^{n+1/2}{}_{i,j_1+1/2,k}\right]_{update\ as\ Eqn(5)}+\frac{\Delta t}{\mu_0\Delta}E_{x,inc}^{\ n}{}_{j_1}$$

$k=k_0-1/2$ Face: H_y ($i=i_0+1/2$,.....,$i_1-1/2$; $j=j_0$,.....,j_1; $k=k_0-1/2$)

$$H_{y}^{n+1/2}{}_{i,j,k_0-1/2}=\left[H_{y}^{n+1/2}{}_{i,j,k_0-1/2}\right]_{update\ as\ Eqn(5)}+\frac{\Delta t}{\mu_0\Delta}E_{x,inc}^{\ n}{}_{k_0}$$

$k=k_1+1/2$ Face: H_y ($i=i_0+1/2$,.....,$i_1-1/2$; $j=j_0$,.....,j_1; $k=k_1+1/2$)

$$H_{y}^{n+1/2}{}_{i,j,k_1+1/2}=\left[H_{y}^{n+1/2}{}_{i,j,k_1+1/2}\right]_{update\ as\ Eqn(5)}-\frac{\Delta t}{\mu_0\Delta}E_{x,inc}^{\ n}{}_{k_1}$$

Chapter 5

Parallel FDTD Method and Absorbing Boundary Conditions

5.1 Parallel FDTD method

The FDTD Method is a versatile numerical technique with the major advantages of simplicity in implementation and robust operation. From an engineering point of view, it is advantageous because it can easily compute the transient response and the operational bandwidth of a device. For large electromagnetic problems, like the one in this thesis, a parallel version of the FDTD algorithm is needed to distribute the grid and run the problem on multi-processor computers or computer clusters.

The FDTD technique is inherently parallel in nature. The computational domain is divided into smaller sub-domains and every one of which is assigned to one processor to solve the three dimensional linear dispersive problem in this thesis [9].

5.2 Message Passing Interface (MPI)

MPI is a message passing library specification based on the consensus of the MPI Forum, which has over 40 participating organizations, including vendors, researchers, software library developers and users. MPI is called on within the FORTRAN or C/C^{++} program to exchange data between processors, permitting many processors to work together to collectively solve the FDTD problem. The tangential field components of the domains are passed between the adjacent interfaces at each time step with an appropriate synchronization procedure, which is provided by the message passing interface (MPI)

library. The parallel process between two sub-domains is depicted in the following figure:

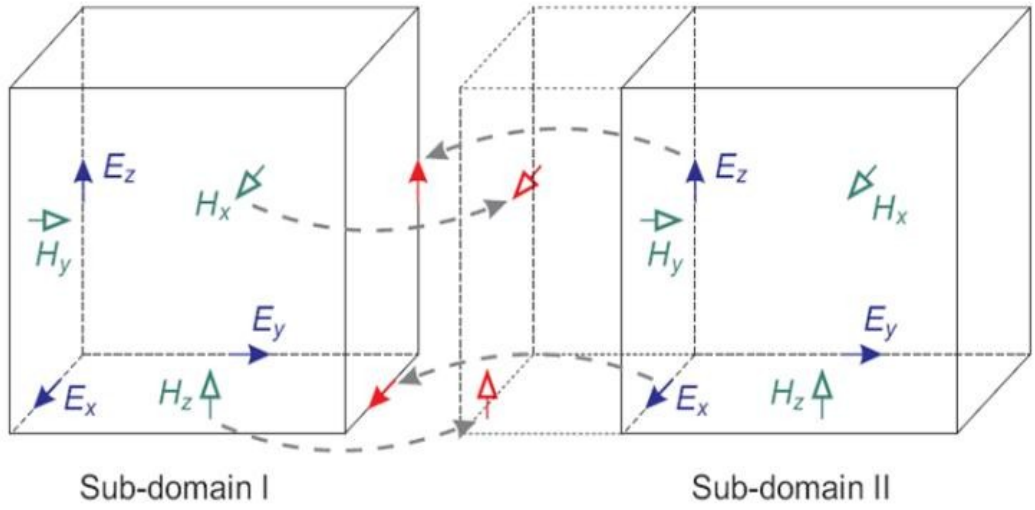

Figure 6: The field components in two different sub-domains in parallel FDTD simulations. The red arrows are the transferred field components from the neighboring sub-domain during the data communication process, which are used to update the field components on the boundary of the current sub-domain (figure courtesy of [9]).

During our simulations, the computational domain is divided in all three directions (x, y and z). Material parameters and the geometry of the simulated device are derived for the whole domain, independently from the parallel procedure.

5.3 Absorbing Boundary Conditions

One of the greatest challenges of the FDTD method has been the efficient and accurate solution of electromagnetic wave interaction problems in the unbounded region. For such problems, an absorbing boundary condition (ABC) must be introduced at the outer lattice boundary to simulate the extension of the lattice to infinity. This approach is also done in this thesis. Berenger's introduction of a highly effective absorbing-material ABC is the perfectly matched layer (PML). The advantage of Berenger's PML is that plane waves of arbitrary incidence, polarization and frequency are matched at the boundary. Berenger derived a novel split-field formulation of Maxwell's equations where each vector field component is split into two orthogonal components. Maxwell's curl equations were also appropriately split, leading to a set of 12 coupled first-order partial differential equations. Then by choosing loss parameters consistent with dispersion less medium, a perfectly matched planar interface is derived. Berenger's split-field PML can be applied directly within an FDTD discretization using a very effective scheme referred to as the convolutional PML (CPML), which has been used in this thesis. The CPML accommodates more general metric tensor coefficients that can lead to improved absorption of slowly varying evanescent waves [1].

Chapter 6

Plasmonic Structures

6.1 Different Plasmonic Structures Used in Photodetectors

Resonant antennas can confine strong optical near fields in a sub-wavelength volume. There are several plasmonic structures that are being used in photodetectors for optical enhancement. Some of them are:

1) Dipole Structure
2) Bow-tie Structure
3) Metal Grating Structure / Bulls Eye Structure
4) Interdigitated Structure
5) Nanopillar, Nanocone, Nanoprism Structure

6.1.1 Dipole Structure

A dipole structure can confine energy in its gap region when it becomes resonant and thereby it can enhance the E-field. For a dipole structure to be resonant the dipole length has to be considerably less than half the wavelength ($L<\lambda/2$), where L is the length of the antenna [10]. Decreasing the gap width increases antenna sensitivity and E-field enhancement in the gap region. Stronger field enhancements can be achieved by decreasing the width of the gap. Intensity enhancement in the dipole gap region is 3 times higher than bow tie antenna [11]. Different shapes of the dipoles have been modeled so far, i.e. rectangular, disk shape, capsule shape, C-shaped dipole structure, etc. These structures are polarization dependent.

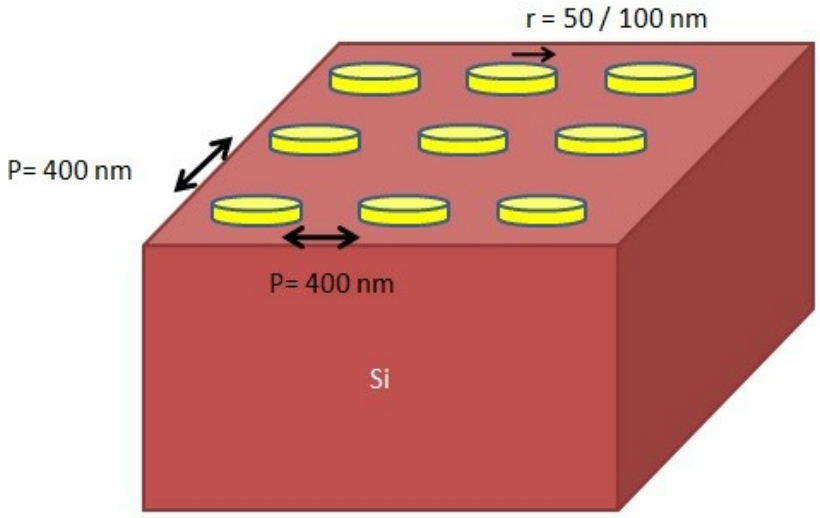

Figure 7: Structure with disk shaped dipoles.

6.1.2 Bow tie Structure

Bow tie structure's field enhancement depends on the antenna length, bow angle α and the gap width. Strongest enhancement is seen when α=90°. The field enhancement is smaller than for a dipole structure but it shows a stronger sensitivity than for dipole structures [11]. The resonance shifts linearly with antenna length for dipole antenna, but this trend is less obvious for the bow tie antenna. Spectral position of the resonance depends much stronger on the gap width for dipole structure than the case of bow tie antenna, where almost no spectral shift can be observed [11].

6.1.3 Metal Grating Structure

Subwavelength plasmonic grating structures have been identified as promising candidates for realizing high speed metal-semiconductor-metal photodetectors (MSM-PDs). FDTD simulations have shown that implementation of grating structures symmetrically about an aperture significantly increases the absorption cross section of the detector, which is defined as the total power absorbed by the detector material in the aperture [12]. The grating structure gives absorption enhancement because each groove of metal grating enhances the propagating evanescent field added to the incident E field [13]. The enhancement depends on the metal grating period and also depends on the slit size (slit width < $\lambda/2*n$), where, n= index of the substrate under the slit) [4]. Grating structures can be concentric; situation typically termed a bull's eye. Rectangular metal grating structures are polarization-dependent, however concentric-grating structure provides polarization-independent enhancement.

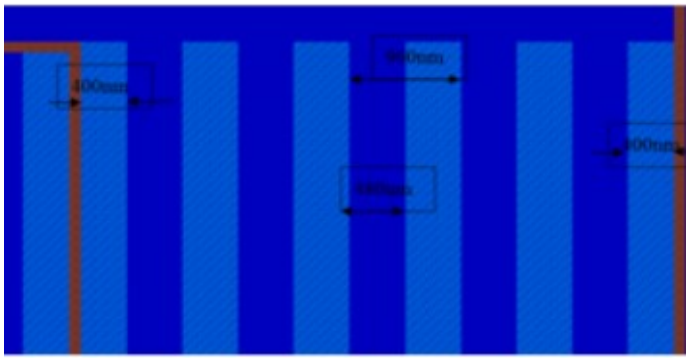

Figure 8: Rectangular metal grating structure (red line indicates slits) (figure courtesy of [13]).

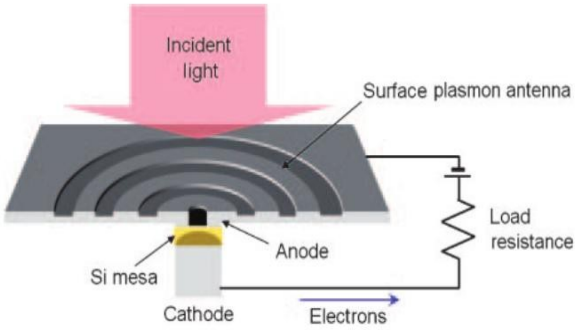

Figure 9: MSM PD with concentric metal grating plasmonic structure (figure courtesy of [4]).

6.1.4 Nanopillar, Nanocone and Nanoprism Structure

The presence of nanostructures like nanopillars, nanocones and nanoprisms reduces the optical reflection and increases absorption as compared to flat cell geometry. Nanocones and nanoprisms have 95% absorption and nanopillar array shows 90% absorption for solar cells [14]. This structure has not yet been modeled for photodiode but has very good potential application for absorption enhancement.

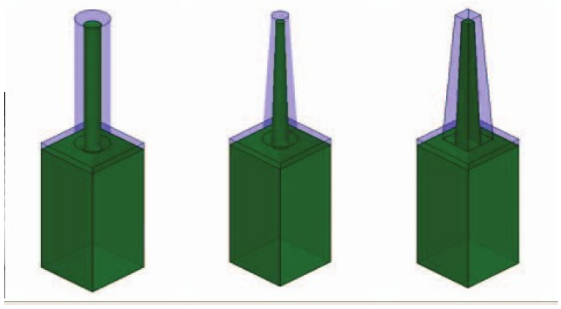

Figure 10: Nanopillar, nanocone and nanoprism structure (figure courtesy of [14]).

6.1.5 Interdigitated Structure

The implementation of interdigitated electrodes in metal-semiconductor-metal (MSM) photodetectors has led to a huge increase in the bandwidth and reduction in dark current, in comparison to a standard PIN photodiode with same active area. Speed of interdigitated plasmonic enhanced MSM-PD is transit time limited but if the length of overlap is considerably large then the capacitance of the device gets increased and the total bandwidth in that case can be capacitance limited [15].

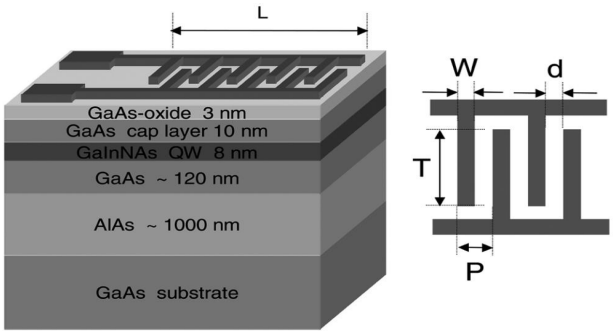

Figure 11: MSM-PD with interdigitated plasmonic structure (figure courtesy of [15]).

Chapter 7

Plasmonic Enhanced Devices

7.1 Photodetector Enhanced by a Near-infrared Dipole Antenna

The speed of the photodiode is limited primarily by the transit time of photogenerated carriers to the electrodes and the depletion-layer capacitance of the semiconductor. Therefore the photodiode can be made intrinsically faster by use of a small active region. A photodetector can be made smaller by using a sub-wavelength active region to increase its speed; however this can result in very low responsivity. Light localized in the optical near field about nanometallic structures has the potential to overcome the trade-off between speed and responsivity by strong optical near-field enhancement [4]. Here we exploit the idea of a half-wave Hertz dipole antenna (length~370 nm) at near infrared wavelengths (~917 nm), to concentrate radiation into a nanometer scale photodetector [6]. The interaction of light with nanostructured metal results in a two to three order intensity enhancement in near-field over the incident field, which is shown in the results. Resonant optical antenna can confine strong optical near fields in a sub-wavelength volume, which has been recently demonstrated for bow-tie and dipole antennas at visible wavelengths [5]. Using the principle of high field enhancement by an antenna, we present a silicon pn photodetector and a subwavelength germanium (Ge) MSM photodetector.

7.2 E-field Enhancement in a Bulk Substrate Si Photodetector

To demonstrate the idea of a nanometallic-structure-enhanced photodetector, we designed a simple aperture experiment with Au dipole antenna on the top of a Si substrate. The

following figure shows the schematic of the device structure.

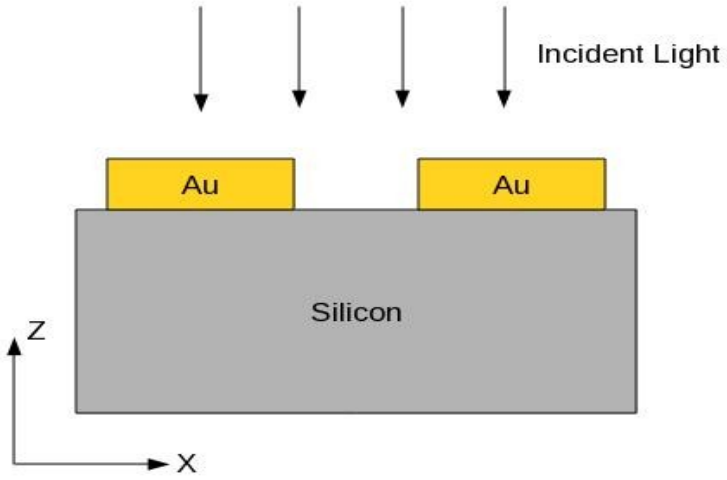

Figure 12: Schematic of the device with bulk Si substrate (cross-sectional view).

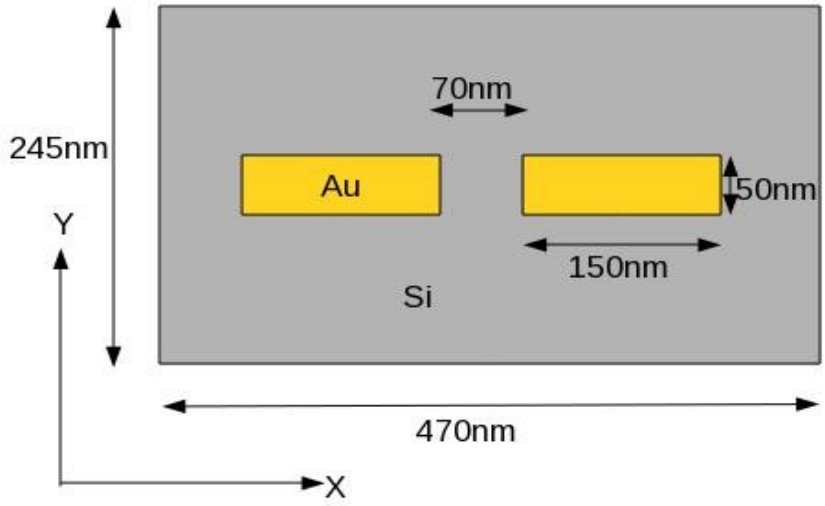

Figure 13: Schematic of the device with bulk Si substrate (top view).

We choose the length and width of the device considering semi-infinite in each

directions. At first x polarized light at wavelength of 500-1550 nm is incident upon the aperture. The metal arms are 50 nm wide, 50 nm thick and 150 nm long and the gap between the two metal arms was 70 nm. We choose the thickness of the gold nano antenna as 50 nm, which is much larger than the skin depth, so that metal is opaque to the incident light [5]. We sample the E-fields in the gap region and we take the DFT of the E-field sampled to get the spectrum. The spectrum we get is given below:

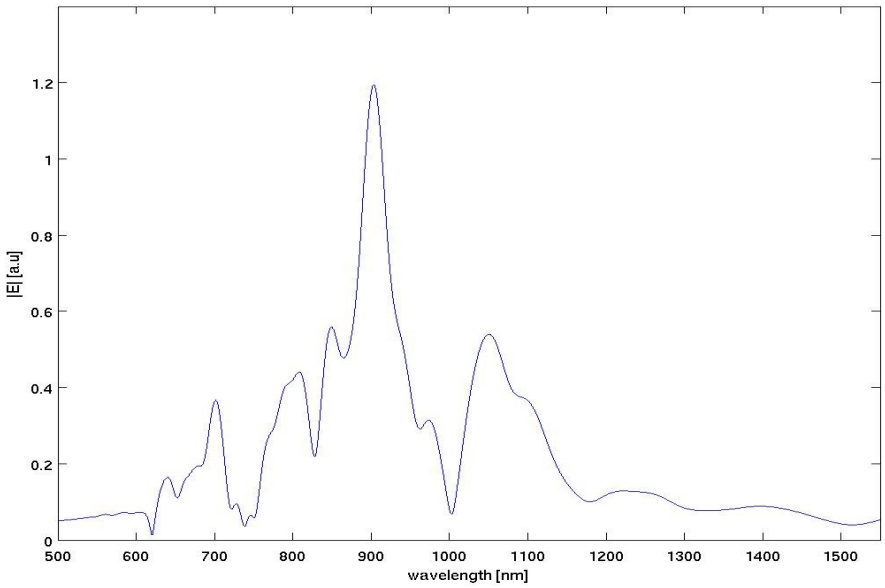

Figure 14: Spectrum of the device with bulk Si substrate (E-field sampled in the gap region).

From the above figure, we see that the maximum enhancement occurs at 904 nm. Here, we are using Si as our substrate, which has a high dielectric constant (ε_r=11.6964), which reduces the E-field enhancement significantly in the gap region. This is because of the

high refractive index mismatch between air and Si. Hence the overall resonant strength of the device is weakened due to the refractive index mismatch. To illustrate this point, we take the FDTD simulated optical near field intensity 25 nm above the substrate surface at wavelength 904 nm, which is given below:

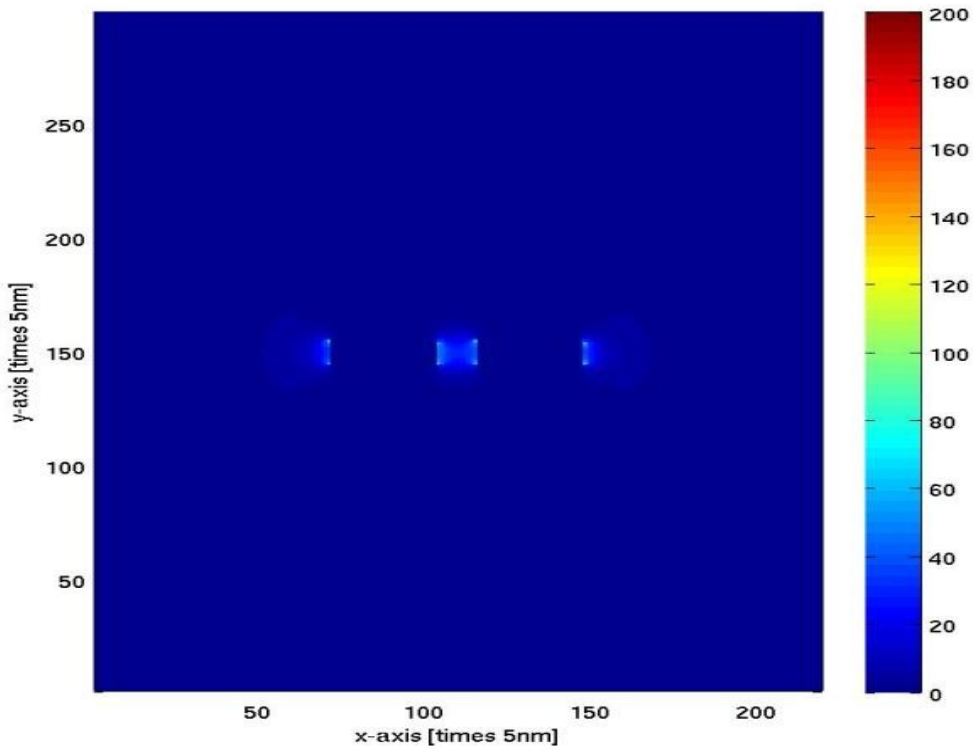

Figure 15: FDTD simulated optical near field intensity ($|E|^2$) 25 nm above the substrate in the x-y plane (resonant at 904 nm).

From the near field intensity diagram we see that there is no significant E-field enhancement neither in the gap region nor around the dipole arms. Now if we see the near field intensity under the gap region in the x-z plane:

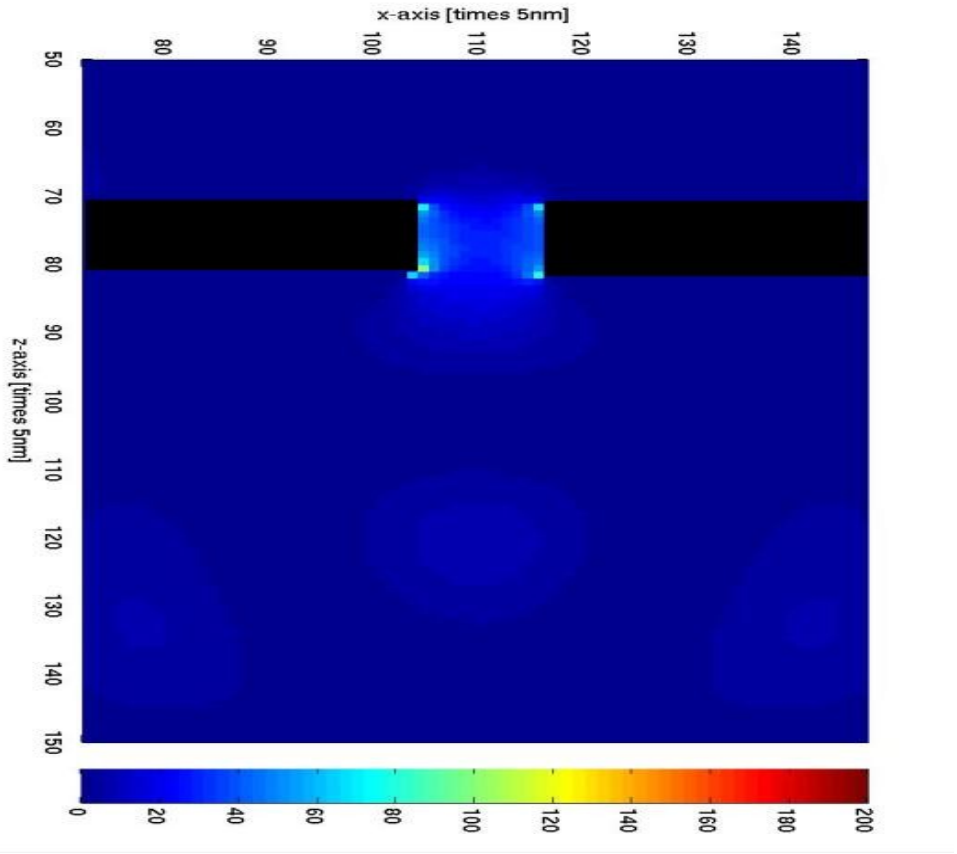

Figure 16: FDTD simulated optical near field intensity ($|E|^2$) in the x-z plane, the dipole arms indicated by black color.

We see that there is no significant E-field enhancement in the gap region and almost the same amount of E-field enhancement underneath the antenna is visible, which again decreases significantly within 50 nm into the substrate. Taking the DFT of the sampled E field, the spectrum of the E field 200 nm under the dipole antenna is given below:

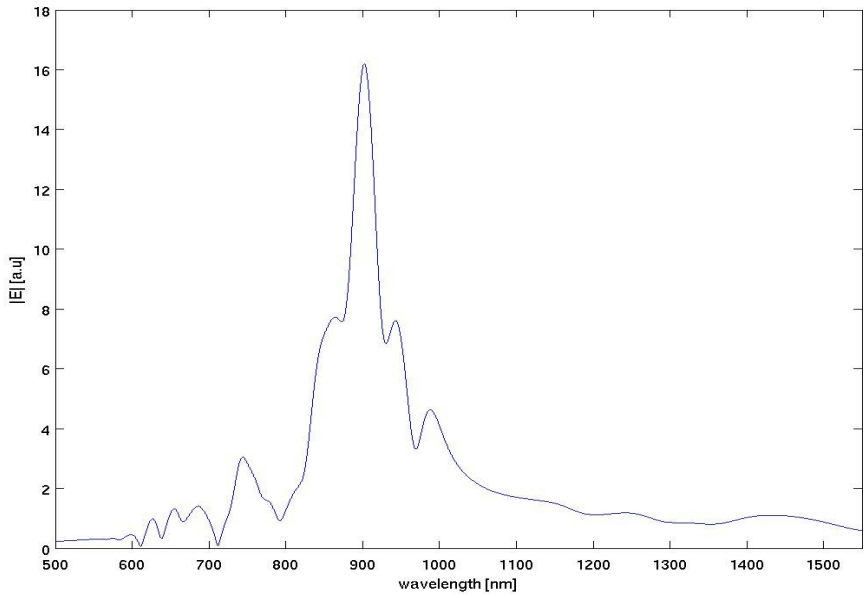

Figure 17: Spectrum of the device with bulk Si substrate (E-field sampled at 200 nm under the dipole antenna).

From the intensity figure in the x-z plane, we see that the intensity enhancement at the resonant wavelength (904 nm) is almost 40 times larger than in the incident E-field intensity at 200nm depth. We therefore conclude that for a material with high dielectric constant with metallic dipole antenna can enhance the E-field under the antenna, which can be used to enhance the photocurrent of an ultra-small photodetector as well as speed, which is dependent upon the area of E-field concentration [4, 16].

Now to overcome the effect of refractive index mismatch, we include a thin (100 nm) SiO_2 layer which has a refractive index of 1.44 underneath the dipole antenna and sample the E-field in the gap region for wavelengths of 500-1550 nm [5]. The device structure is

given below,

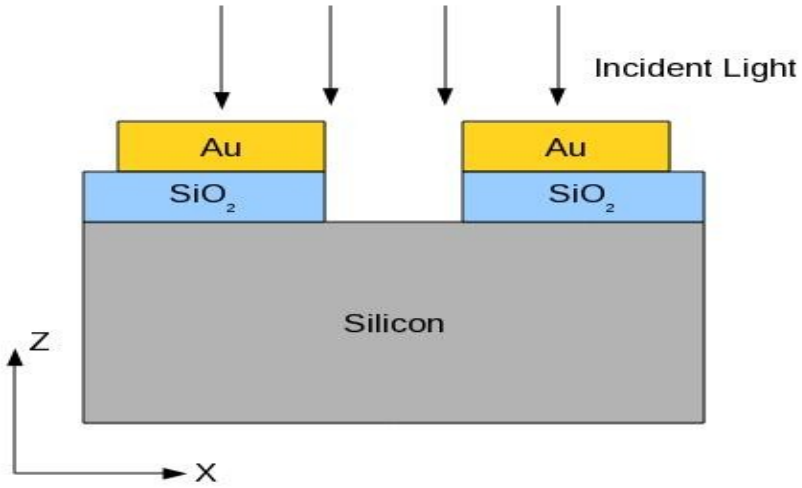

Figure 18: Schematic of the device with bulk Si substrate and thin SiO_2 underneath the antenna arms (cross-sectional view).

The E-field spectrum in the gap region in this case given below:

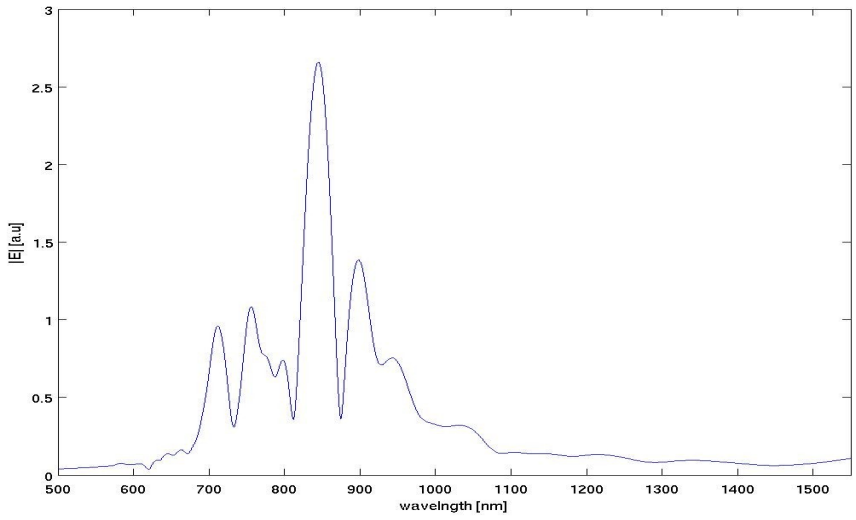

Figure 19: Spectrum of the device with bulk Si substrate and thin SiO_2 underneath the antenna arms (E-field sampled in the gap region).

If we compare this spectrum with the spectrum of the device without SiO_2 layer, we see that the resonance has been shifted to 845 nm and the E-field enhancement is doubled at resonance in this case when compared to the previous one. Again if we see the spectrum of this aperture at 200 nm under the antenna in to the substrate, we get the following spectrum:

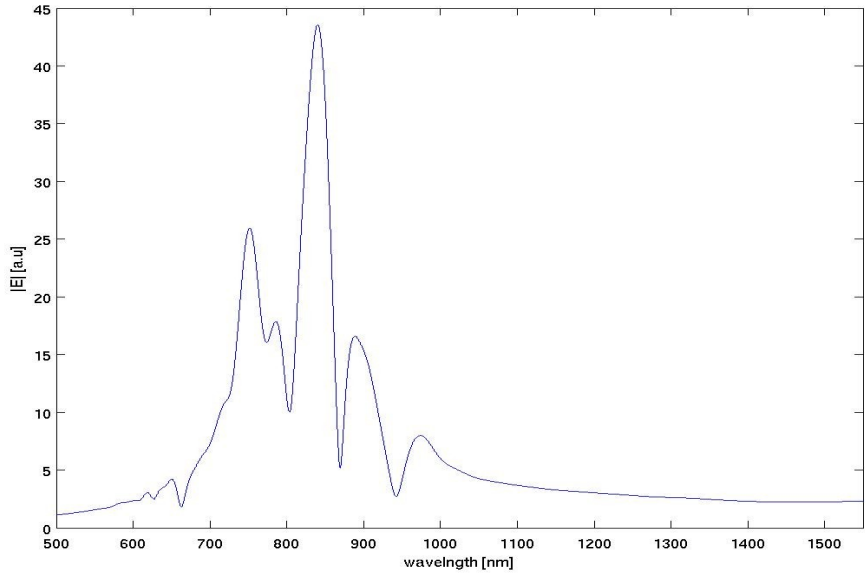

Figure 20: Spectrum of the device with bulk Si substrate and thin SiO_2 underneath the antenna arms (E-field sampled at 200 nm under the dipole antenna).

If we compare this one with the case of the structure without SiO_2 shown previously, we see an enhancement of which is almost doubled inside the substrate compared to case with only Si layer at resonance. From this we can conclude that, with SiO_2 layer, even though we move to a smaller resonant wavelength, there is a significant increase in E-field enhancement inside the material, which can be applicable for designing a

photodetector at visible wavelength with higher responsivity.

7.3 E-field Enhancement in a Germanium Photodetector

Since SiO_2 has a refractive index closer to the air, to overcome the refractive index mismatch issue a thick (1um) SiO_2 layer underneath the dipole antenna is added [5]. The device structure now is shown below:

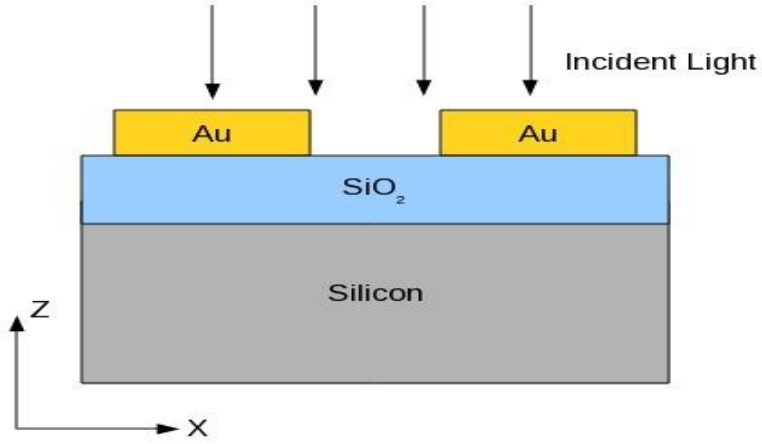

Figure 21: Schematic of the device without Ge and with thick SiO_2 substrate (cross-sectional view).

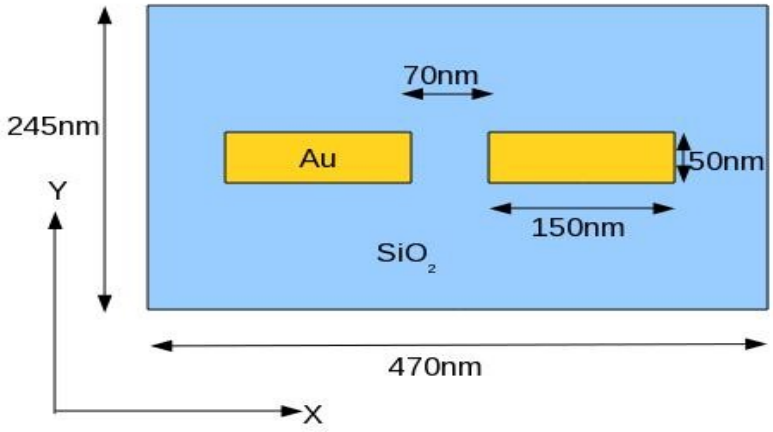

Figure 22: Schematic of the device without Ge and with thick SiO_2 substrate (top view).

We choose the length and width of the device considering semi-infinite in each directions. In all the configurations our metal arms are 50 nm wide, 50 nm thick and 150 nm long. We incident x polarized light upon our structure of wavelength 500-1550 nm as the device gives maximum enhancement when the light is polarized parallel to the antenna arm [7]. The E-fields are sampled in the gap region to find the resonance. The sampled E field in the gap region in time domain is given below:

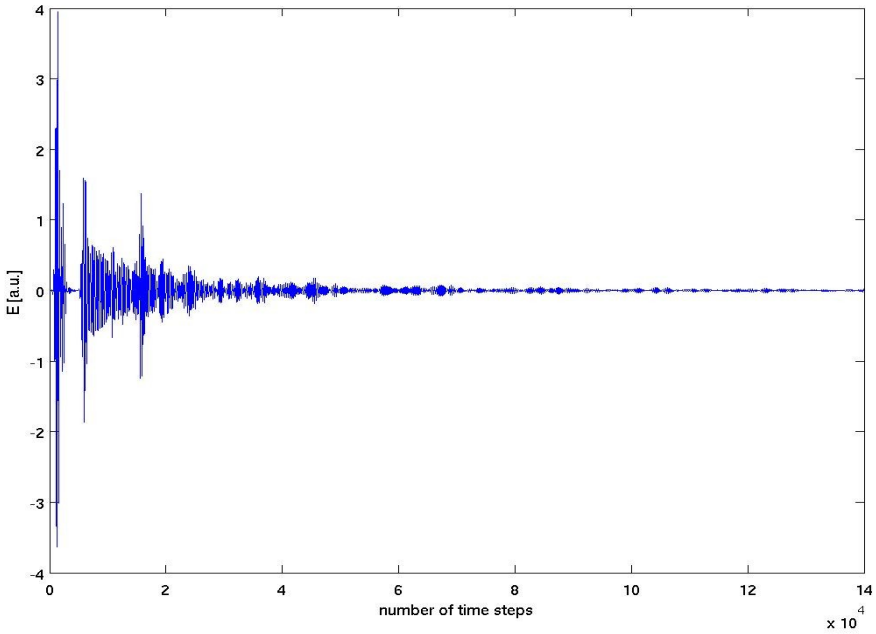

Figure 23: Sampled E-field time waveform.

Here, each time step is 9.532×10^{-18} s long. To make the E-field to go completely to zero, we applied a decaying Gaussian exponential for last 20,000 time steps.

After taking the DFT, we get the following spectrum:

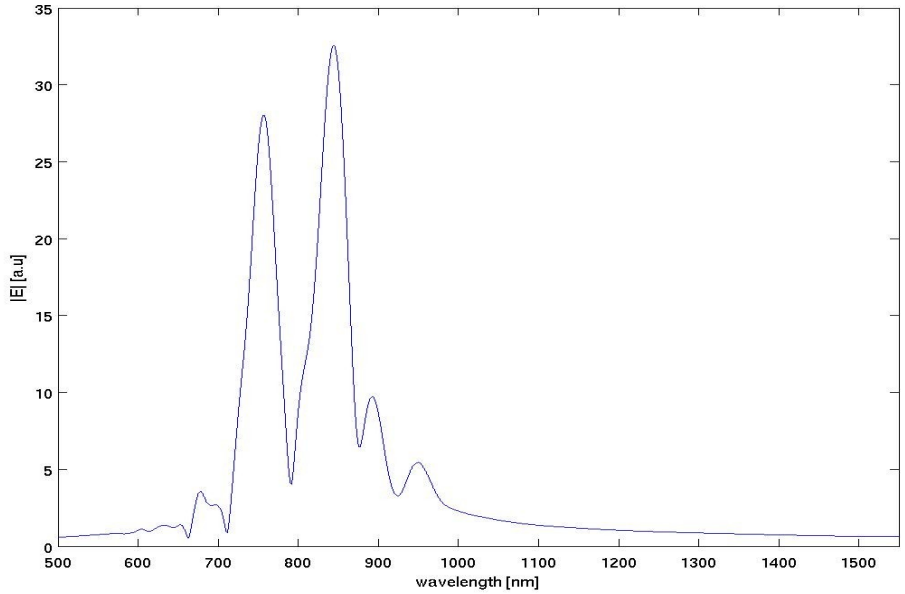

Figure 24: Spectrum of the device without Ge and with thick SiO_2 substrate (E-field sampled in the gap region).

From the spectrum we find the maximum E-field enhancement at 845 nm, which is the resonance in this case. The dipole antenna length determines the resonance of the antenna. But with dipole antenna, the SiO_2 and Si substrate the resonance is 845 nm, which is more than two times the antenna length (370 nm).

Now FDTD simulated optical near field intensity 25 nm above the substrate at 845nm wavelength is given below:

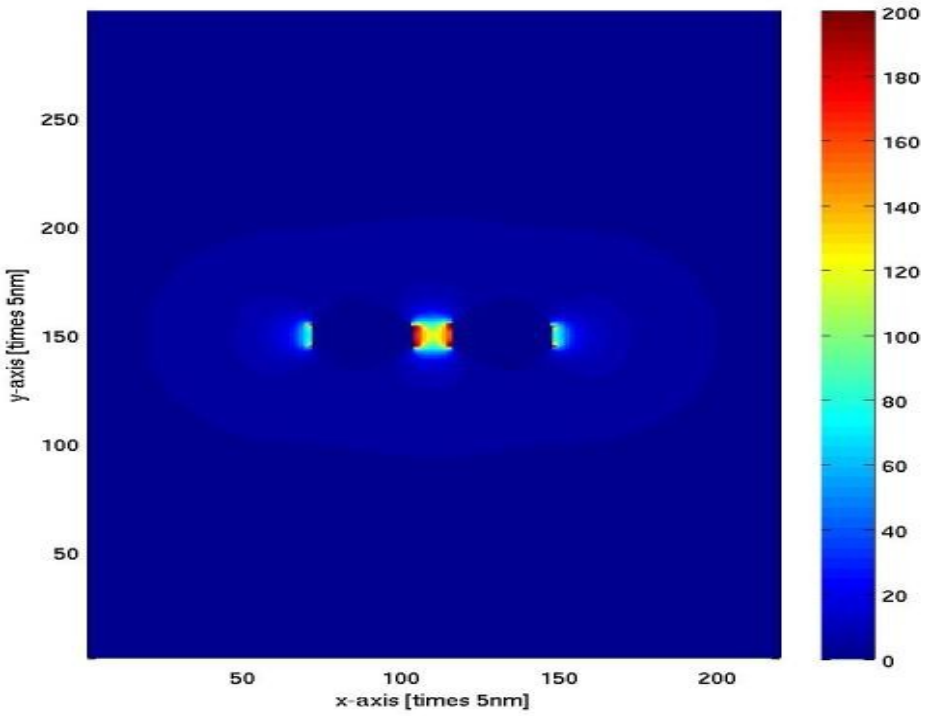

Figure 25: FDTD simulated optical near field intensity ($|E|^2$) 25 nm above the substrate in the x-y plane (resonant at 845 nm).

Now we also can obtain the FDTD simulated near-field intensity in the x-z plane, which is given below:

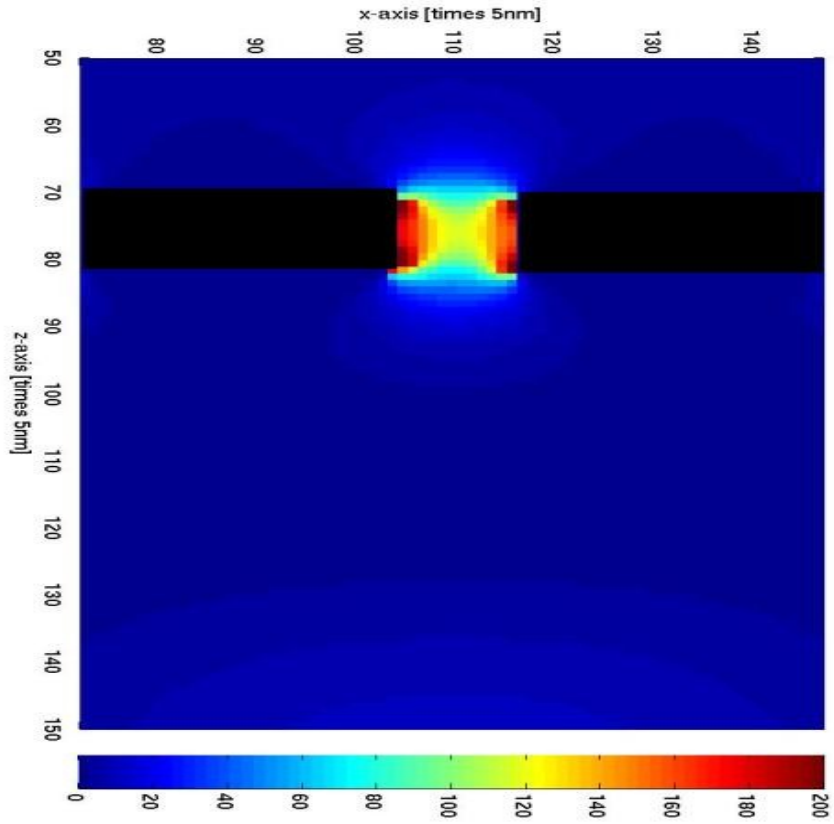

Figure 26: FDTD simulated optical near field intensity ($|E|^2$) in the x-z plane, the dipole arms indicated by black color.

From the above two simulations we can conclude that after refractive index matching using SiO_2 layer, we get a 2 to 3 order of E-field enhancement in the gap region. To get a considerably large increase in responsivity of a photodetector, we definitely would like to use that enhancement. To do so, we need to implement our active device in this region.

So, to achieve that purpose we add Ge in the gap region and the device structure is given below:

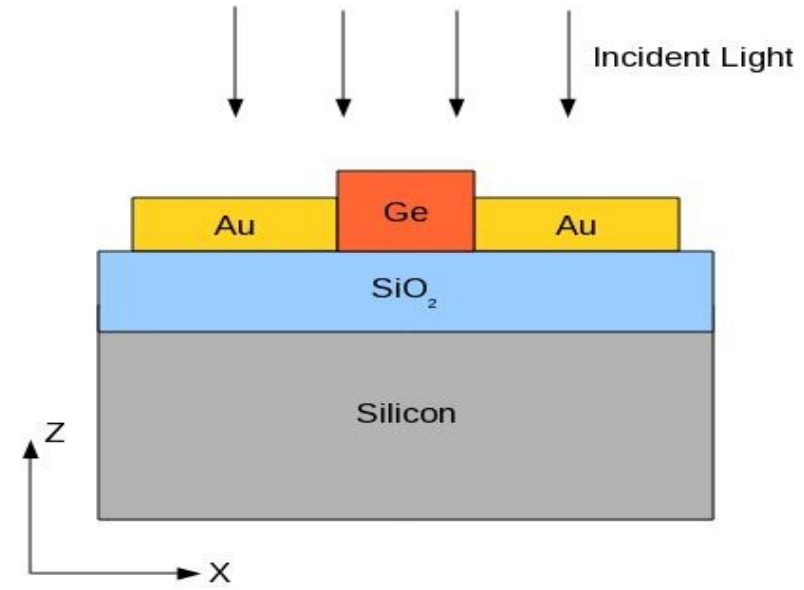

Figure 27: Schematic of the device with Ge in the gap region and with thick SiO_2 substrate (cross-sectional view).

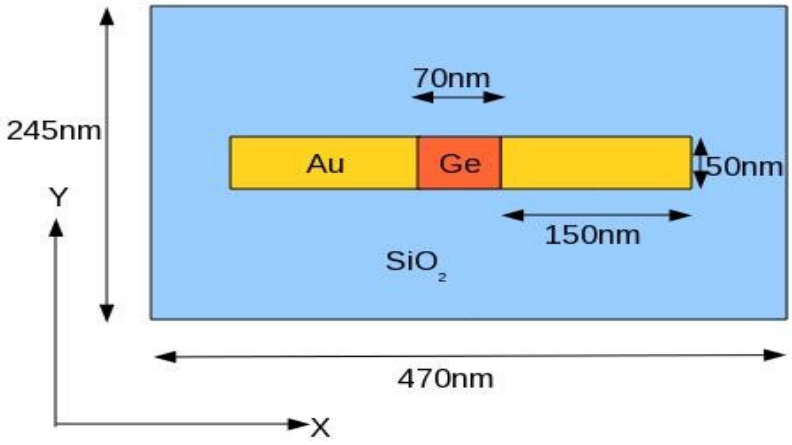

Figure 28: Schematic of the device with Ge in the gap region and with thick SiO_2 substrate (top view).

The incident wave is x-polarized light in the wavelength range of 500-1550 nm, the E-field sampled inside the Ge and the Ge layer is 75nm thick. Taking the DFT of the time waveform of the sampled E-field, we get the following spectrum:

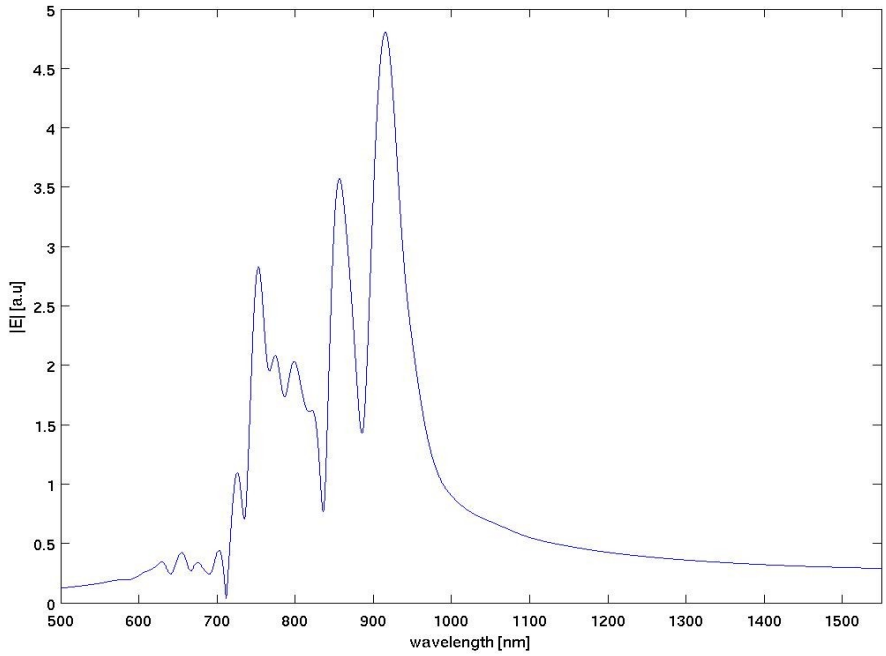

Figure 29: Spectrum of the device with Ge in the gap region and with thick SiO_2 substrate (E-field sampled in the gap region).

Here, we see the maximum E-field enhancement occurs at 917 nm, which is the resonant wavelength. The resonance has been shifted to a higher wavelength. Resonance shifts to higher wavelength and resonant strength has been weakened due to high dielectric constant of Ge (ε_r =19) [5]. So, we conclude that high dielectric constant material shifts resonance to higher wavelength and weakens the resonant strength.

Now the FDTD optical near-field intensity in the x-y plane at resonance is given below:

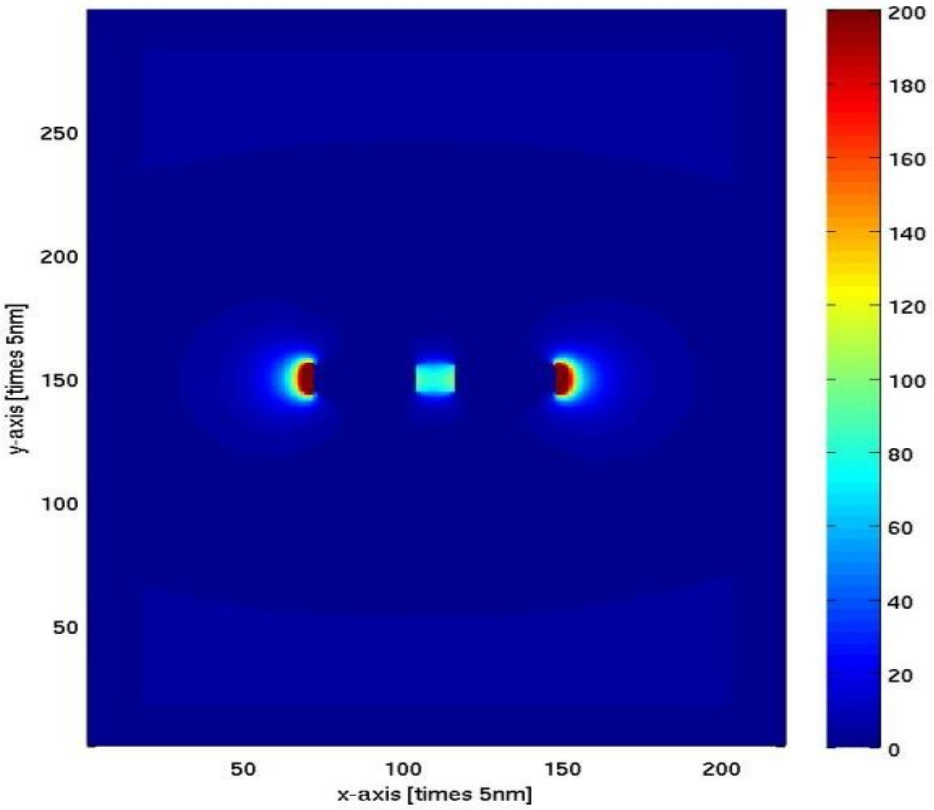

Figure 30: FDTD simulated optical near field intensity ($|E|^2$) 25 nm above the substrate in the x-y plane (resonant at 917 nm).

The E-field around the antenna indicates large capture area of light in the device. Note, for the Ge in the gap region, the maximum E-field is at the two ends of the antenna arms, while the highest energy is still concentrated in the gap owing to the high dielectric constant of Ge as the energy is proportional to ε times the magnitude square of the E field. Our device is resonant at 917nm, as we are considering a bulk substrate. So to make

the device resonant at optical frequency (1310 nm), we have to make our device smaller.

7.4 Effect of Gap Size and Thin Element on E-field Enhancement and Resonance

To show the effect of gap size and using thin element instead of a bulk substrate on E-field enhancement and resonance, we use the following device structure.

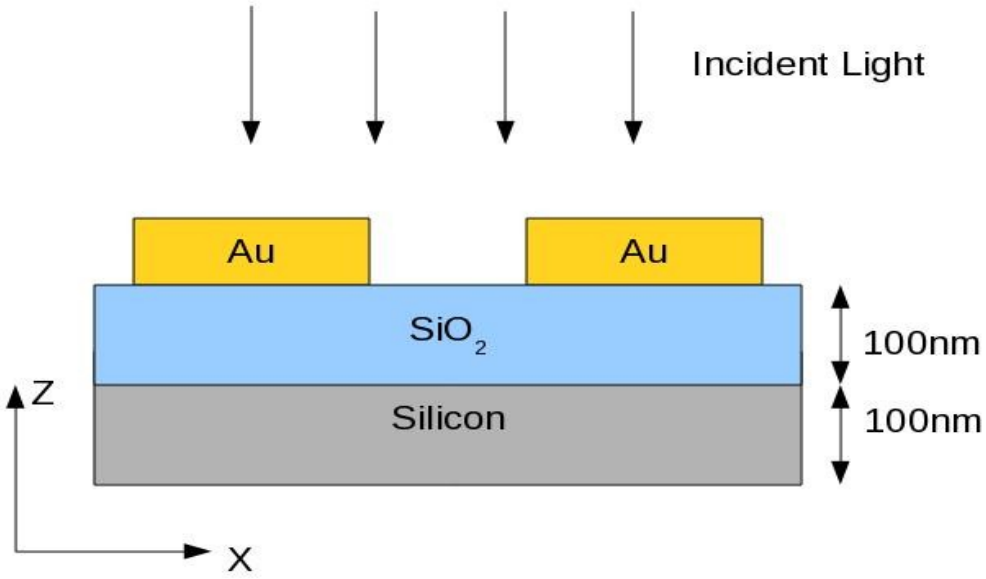

Figure 31: Schematic of thin element device structure without Ge (cross-sectional view).

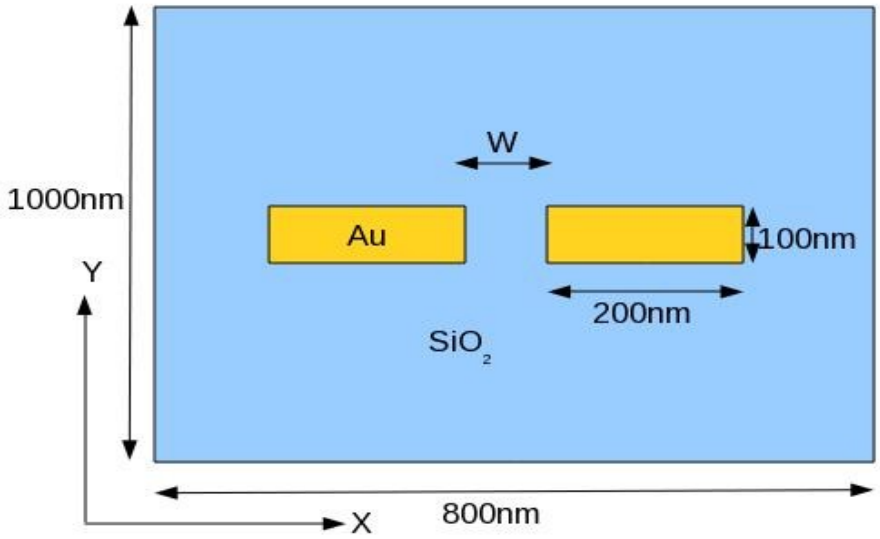

Figure 32: Schematic of thin element device structure without Ge (top view).

We choose the length and width of the device considering semi-infinite in each directions. Here, we have chosen the thickness of the SiO_2 and Si layer as 100 nm each, which we considered a thin element and we probe to analyze the spectrum for different gap size, W. The metal arms are 100nm wide, 30 nm thick and 200nm long. The gap size has been varied in steps such that 100 nm, 200 nm and 300 nm, respectively, are achieved. The incident light is x polarized of wavelength 500-1550 nm. We sampled the E-field in the gap region and took the DFT of it to get the spectrum.

The spectrum for W=100 nm is given by,

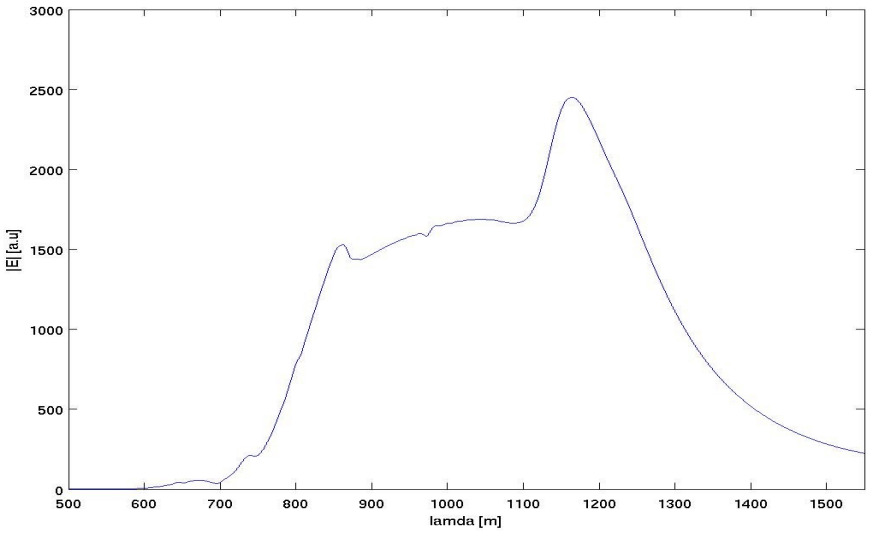

Figure 33: Spectrum of the thin element device without Ge and gap size = 100 nm (E-field sampled in the gap region).

From the above curve we see the resonance is at 1164 nm. Now let's see the spectrum for gap size, W=200 nm:

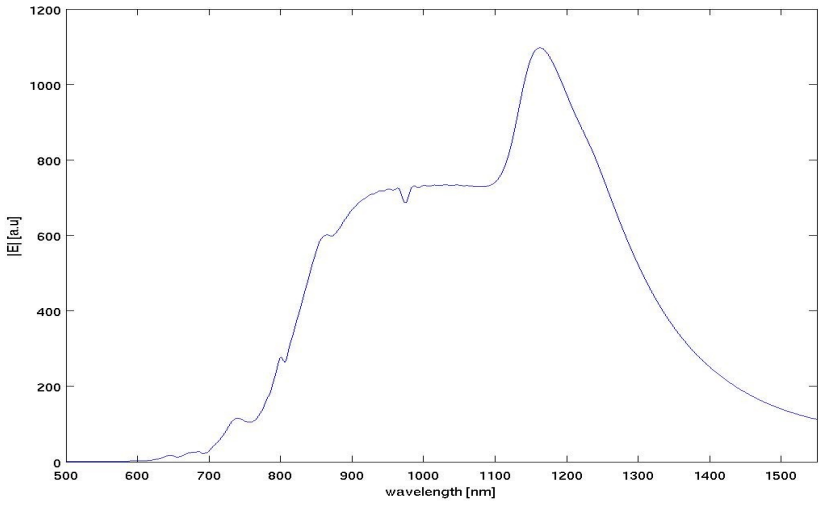

Figure 34: Spectrum of the thin element device without Ge and gap size = 200 nm (E-field sampled in the gap region).

From the above curve we see the resonance is at 1163 nm. Now let's see the spectrum for gap size, W=300 nm:

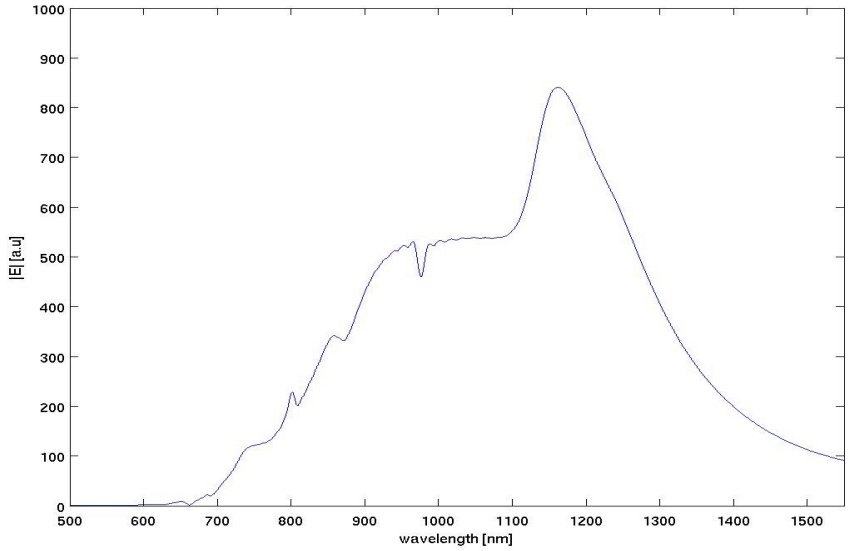

Figure 35: Spectrum of the thin element device without Ge and gap size = 300 nm (E-field sampled in the gap region).

From the above curve we see the resonance is at 1161 nm. Now we add 100 nm wide, 100 nm long and 60 nm thick Ge element in the 100 nm gap region and we get the following spectrum, sampling the E-field in the Ge region:

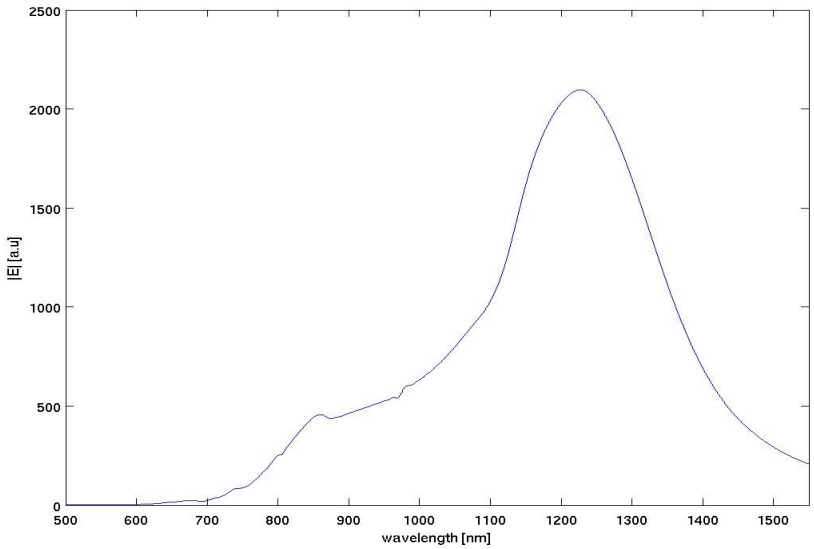

Figure 36: Spectrum of the thin element device with Ge and gap size = 100 nm (E-field sampled in the Ge region).

From the above curve, the resonance shifts to 1225 nm. Thus, we conclude that, as gap size increases, the maximum E-field enhancement decreases, which behaves according to the theory. Further, as we add Ge in the gap region, the resonance shifts 61nm. But, if we compare thin element resonance with the resonance of the previous structure featuring the bulk substrate, we see that, with a thin element, our resonance shifts to a higher wavelength [5]. And resonance shifts after adding Ge, in this case (61 nm), is smaller than in case of structure with bulk substrate (72 nm). This can be utilized to design a photodetector for optical wavelengths (1310 nm / 1550 nm) as thin element device shifts the resonance to a higher wavelength according to FDTD. To design a photodetector for optical wavelengths (1310 / 1550 nm), we need to make our device smaller.

Chapter 8

Nanojet Enhanced Devices

8.1 Photonic Nanojets

The photonic nanojet is a narrow, high-intensity electromagnetic beam that propagates into the background medium from the shadow side surface of a plane-wave illuminated loss-less dielectric micro-cylinder or micro-sphere of diameter greater than the illuminating wavelength, λ. The transverse beam width of the nanojet can be as small as λ/3, and the longitudinal length can be as long as 20λ [8].

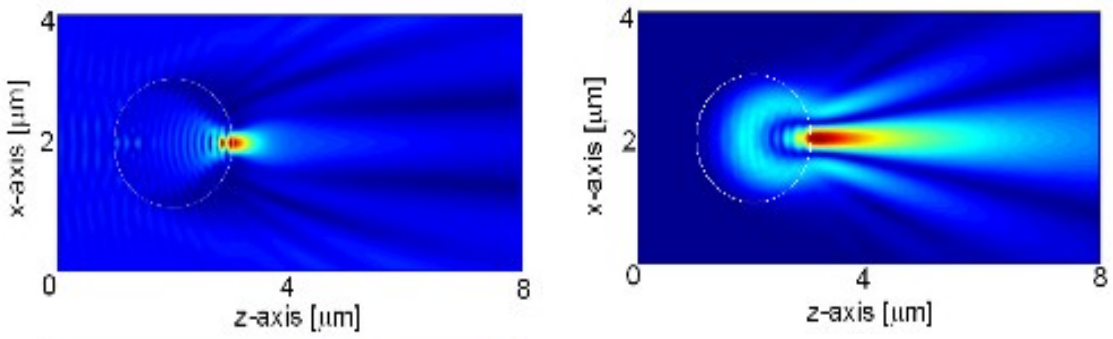

(a) (b)

Figure 37: Photonic nanojet for (a) homogeneous dielectric sphere, (b) optimally graded dielectric sphere (figure courtesy of [8]).

Since, the transverse beam-width of the nanojet can be as small as λ/3, we can use photonic nanojet to concentrate the energy into a small region. We test the use of a photonic nanojet to concentrate the light instead of using the plasmonic structure.

8.1.1 Spectrum of the Nanojet

At first, we begin with checking the photonic nanojet spectrum. From Fig. 38 below, it is found that a sphere with diameter of 6 um has a broad spectrum spread over our wavelength of interest, which is 500-1550 nm. The incident plane wave is x-polarized. The refractive index of the sphere we consider is 1.59. The E-fields are sampled at the center of the nanojet at the point of maximum intensity. The spectrum is obtained by taking the DFT of the time waveform of the E-field.

The spectrum of the photonic nanojet from a 6um diameter sphere is given below:

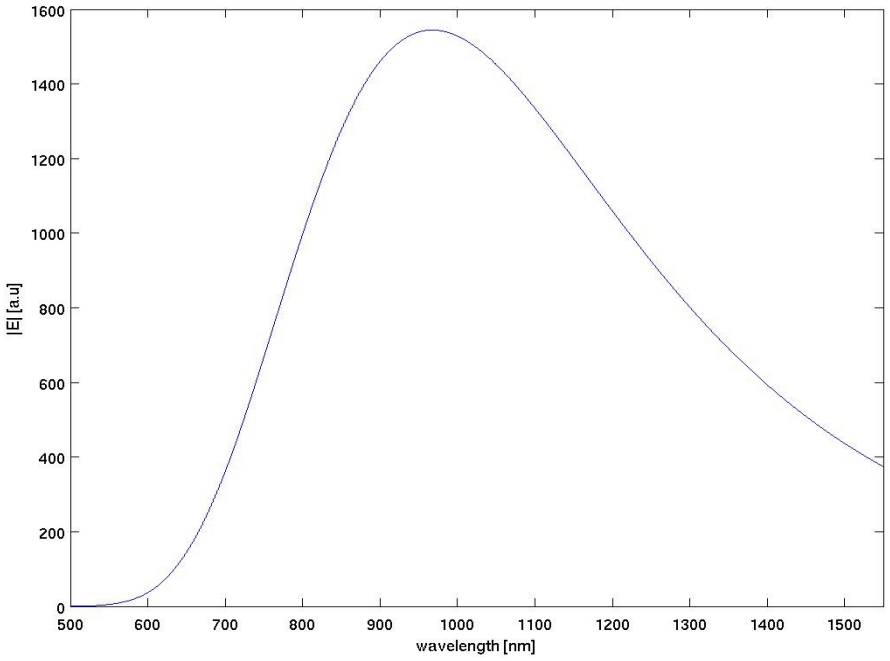

Figure 38: Spectrum of a photonic nanojet of diameter 6 um.

From the above spectrum, we can say that the enhancement becomes maximum at 970 nm but it remains a reasonable value for E-field enhancement upto 1310 nm optical wavelength. We can apply photonic nanojet to visible range using a sphere of diameter less than 5 um as for smaller sphere the maxima shifts towards visible wavelength. And we may shift the maxima towards optical wavelength by increasing the diameter from 6 um, as increasing the diameter shifts the maxima towards higher wavelength.

8.2 Germanium Photodetector Enhanced by Nanojet

To see the E-field enhancement for a device made on a Si substrate, we used the following structure at first:

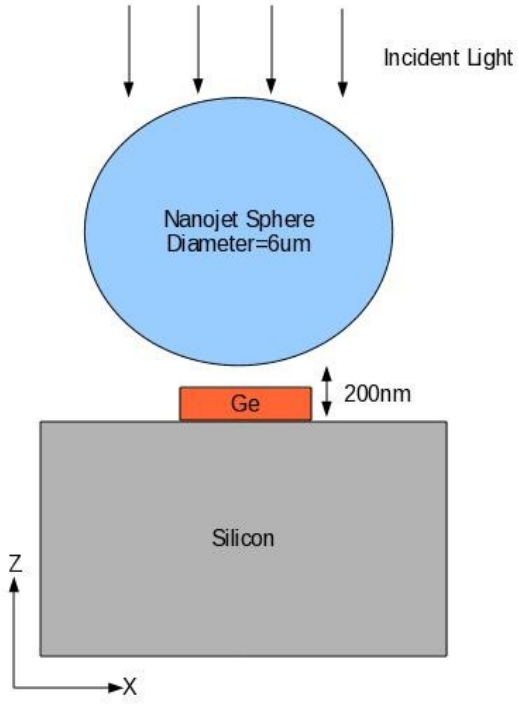

Figure 39: Schematic of the Ge photodetector with nanojet (cross-sectional view).

Here, Ge layer is 200 nm wide, 100 nm thick and 200 nm long, and the Si is a bulk Silicon substrate. The dielectric sphere has a refractive index equals to 1.59. We sample out E-field in the Ge region and take the DFT to see the E-field enhancement.

The Spectrum is given below:

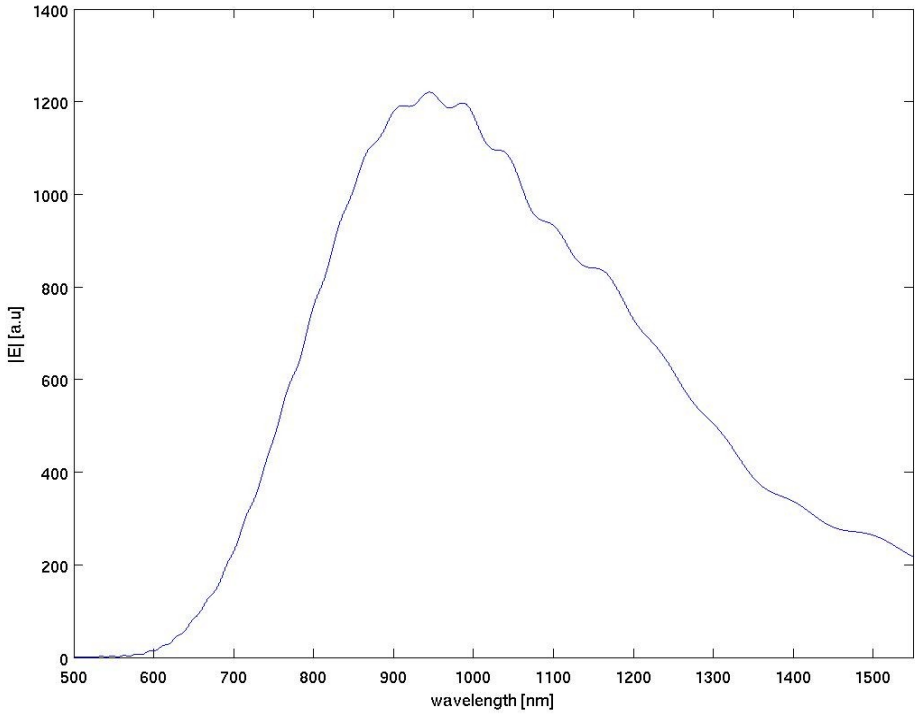

Figure 40: Spectrum of the Ge photodetector with nanojet (E-field sampled in Ge).

From this curve we see that the maximum enhancement is at 945 nm, so the maximum enhancement peak shifts slightly to lower frequency due to reverberations of the electromagnetic wave between the photodetector materials and the sphere.

To examine the effect of refractive index mismatch issue, we considered the following structure:

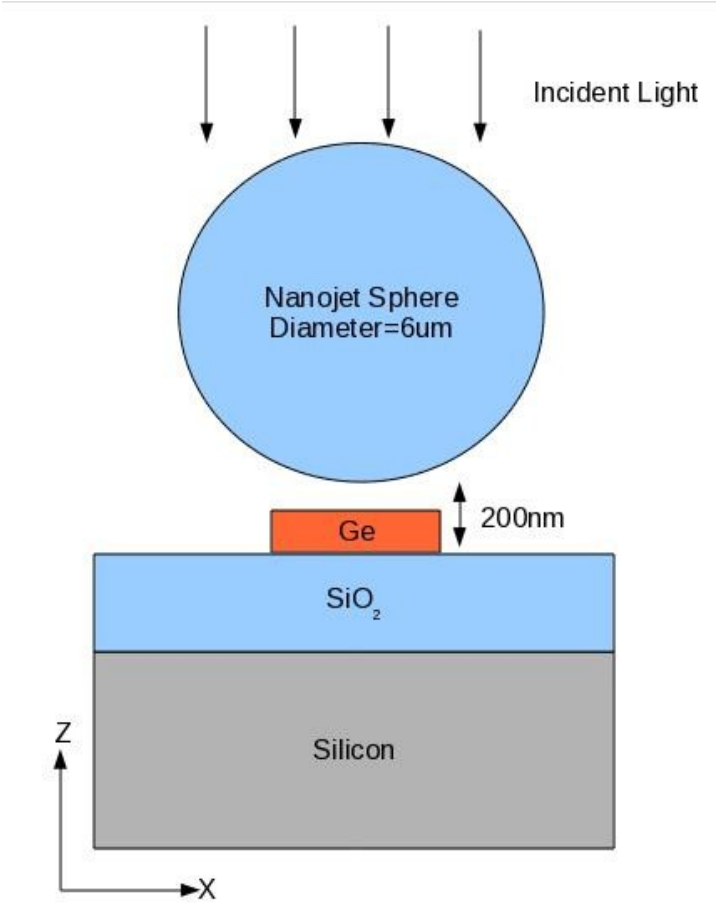

Figure 41: Schematic of the Ge photodetector with nanojet upon a thick SiO_2 substrate (cross-sectional view).

We add a SiO_2 layer which has a refractive index closer to air and equals to 1.44. We again sampled the E-field in the Ge region and took the DFT to get the following spectrum:

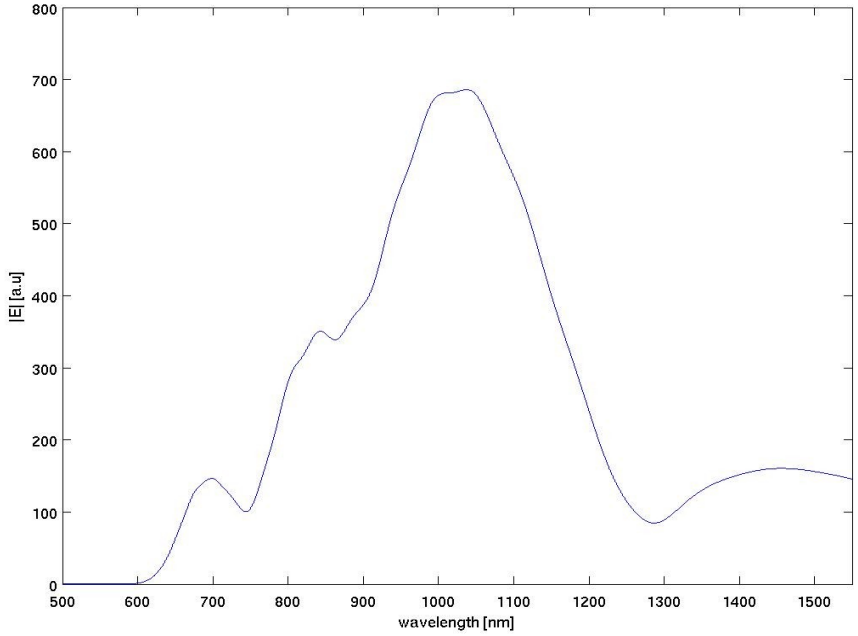

Figure 42: Spectrum of the Ge photodetector with nanojet upon a thick SiO_2 substrate (E-field sampled in Ge).

From the above figure we see that the maximum enhancement shifts upward to a wavelength to 1046 nm but the enhancement is not as large as in the case of a device without refractive index matching. So, to design a photodetector to work at optical wavelength (e.g. 1310 nm), we can use that property as it shifts the maximum E-field enhancement to higher wavelength. But if we want high responsivity then we can use a material with high dielectric constant as our substrate.

To compare the E-field enhancement due to nanojet in the Ge MSM photodetector, we took the FDTD simulated optical near-field intensity due to nanojet on the Germanium without the SiO_2 layer as it gives more enhancement than with SiO_2 layer. The incident light is x-polarized and has a wavelength of 945 nm. The device structure from top view is given below:

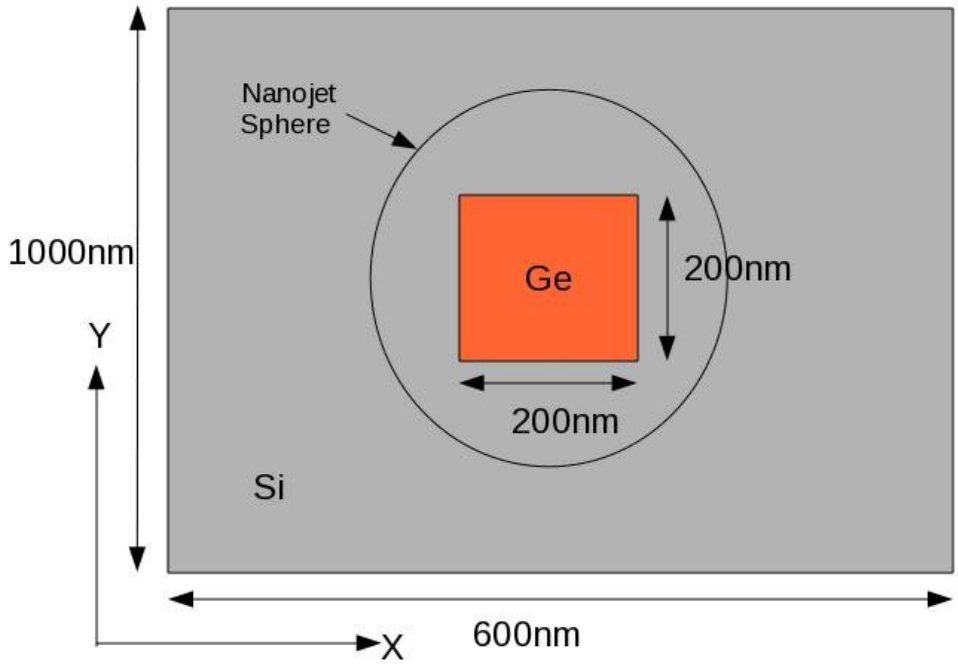

Figure 43: Schematic of the Ge photodetector with nanojet (top view).

The optical near field intensity due to nanojet 50 nm above the Si substrate in Ge is given below:

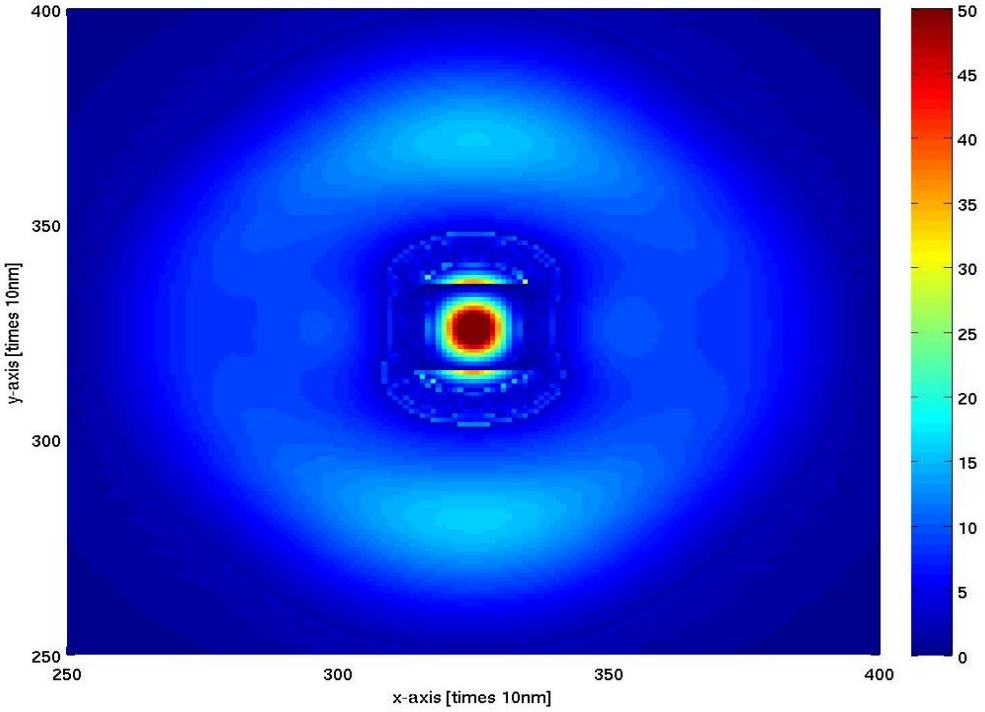

Figure 44: FDTD simulated optical near field intensity ($|E|^2$) 25 nm above the substrate in the x-y plane with nanojet structure.

If we compare the nanojet enhancement with plasmonic enhancement in the Ge of the gap region, we can see that both give almost the same enhancement.

The optical near field intensity for plasmonic enhancement is given below changing the color bar value in the range of 0-50:

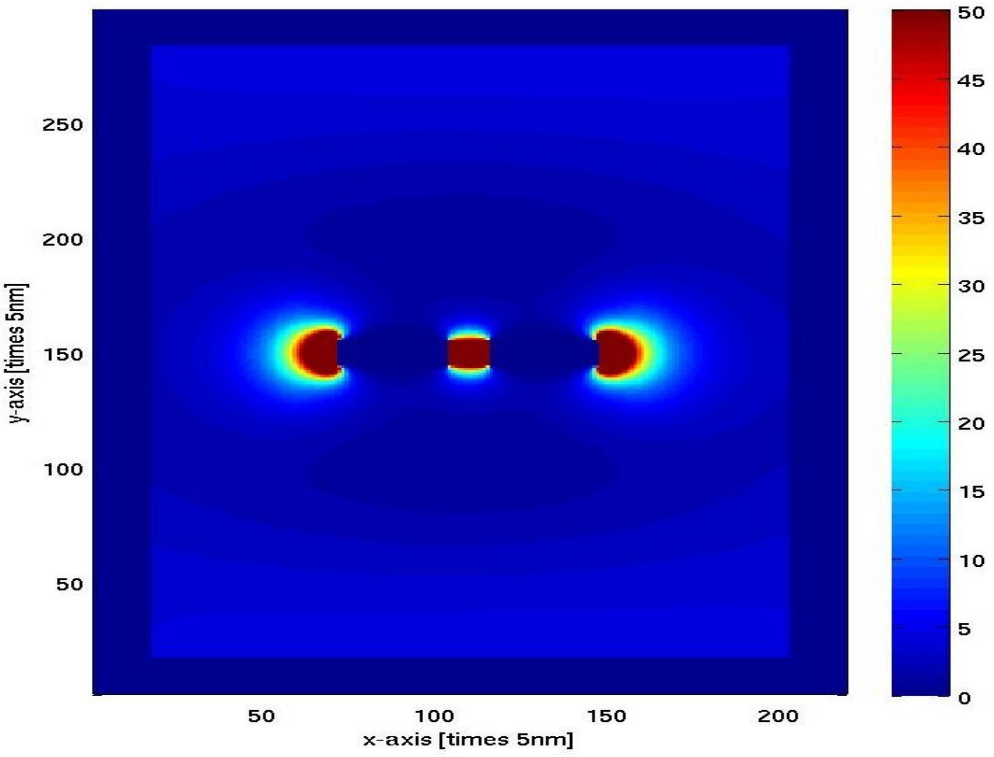

Figure 45: FDTD simulated optical near field intensity ($|E|^2$) 25nm above the substrate in the x-y plane with plasmonic structure.

From the above two figure, we conclude that the optical near field intensity in the Ge region is almost the same by comparing the color bar value. So, the responsivity for both nanojet and plasmonic enhanced photodiode will be almost same. However, we note that the area of Ge in which the plamonic enhanced photodiode is concentrating the E-field has an approximate area of 50x70 nm^2, while the area of Ge in which the nanojet is concentrating the E-field has an approximate area of 200x200 nm^2. Therefore, we can conclude from that the speed will be higher for plasmonic enhanced photo diode as it concentrates the light in a smaller area. Even though the speed of nanojet enhanced

photodiode will not be as great as plasmonic enhanced photodiode but still it will give us much better speed than a simple photodiode. Alternatively, the speed using photonic nanojet can be increased by changing the composition of the nanojet sphere.

8.3 Bulk substrate Si photodetector Enhanced by Nanojet

To compare the bulk substrate Si pn photodiode enhanced by nanojet with that of one enhanced by a plasmonic structure, we consider the following structure:

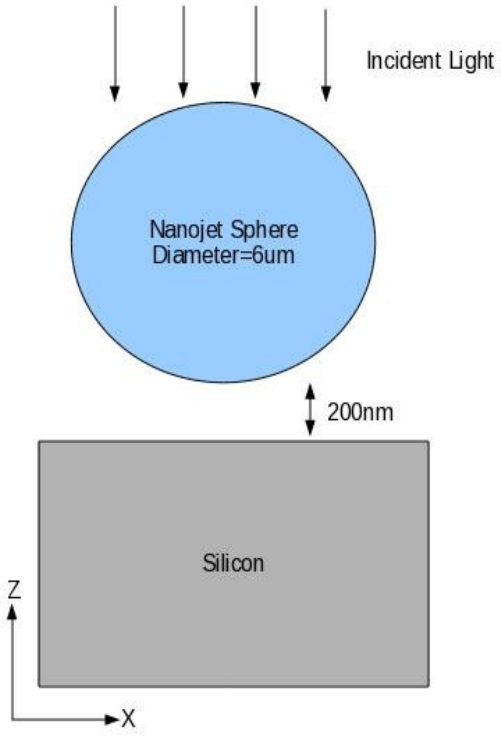

Figure 46: Schematic of the Si photodetector with nanojet (cross-sectional view).

Now the optical near-field intensity in the bulk Si substrate due to nanojet enhancement in the x-z plane is given below:

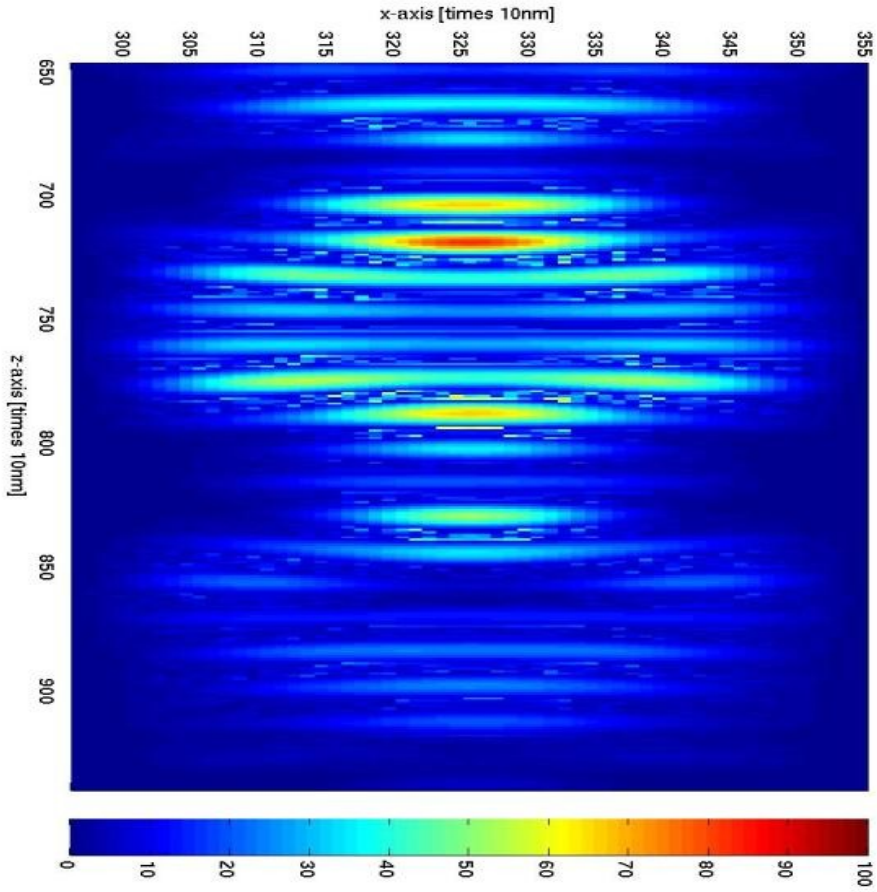

Figure 47: FDTD simulated optical near field intensity ($|E|^2$) in the x-z plane with nanojet structure for Si photodetector.

Here, the x-z cross section has an area of 0.6x3 um^2. From the figure we see a large enhancement in intensity in the x-z plane.

The plasmonic structure enhancement is given below for bulk Si substrate:

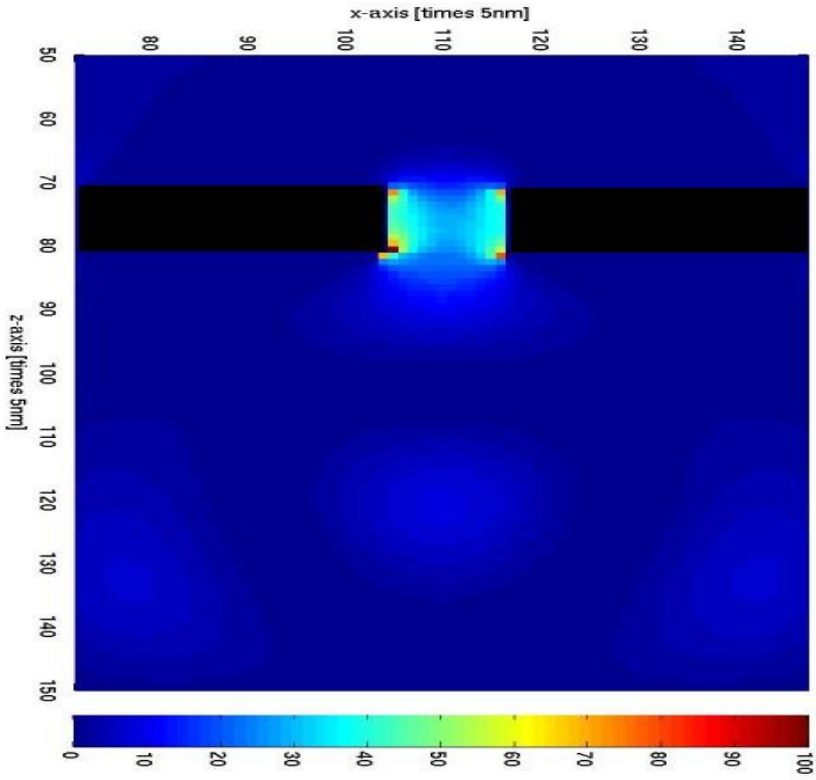

Figure 48: FDTD simulated optical near field intensity ($|E|^2$) in the x-z plane of a bulk substrate Si photodiode, the dipole arms indicated by black color.

We can say that, for a nanojet enhanced Si photodiode, there is a larger enhancement in the intensity in the bulk substrate compared to the plasmonic enhancement case. From this, we can expect a large enhancement in photocurrent due to nanojet compared to plasmonic case for the bulk substrate photodiode. Since the nanojet confines the energy in an area of 200x200 nm^2 as we saw in the case of a germanium photodetector in the x-y plane, the speed will also be improved. The speed can be further improved by changing the composition of the nanojet sphere.

Chapter 9

Conclusion

In this thesis, a thorough study of plasmonic and nanojet enhanced photodetectros was provided. Nano aperture plasmonic near-infrared dipole antenna was shown to enhance the E-fields in a sub-wavelength volume, which can be used to get improved performance from ultra-small pn or MSM photodetectors [16]. Ultra-small MSM-PD has been widely used in high-speed optical receivers because of its easy integration, high-speed and low-capacitance operation [6, 16]. The results were obtained via FDTD modeling involving an incident plane wave by the way of the TFSF technique and also applied CPML absorbing boundary conditions. Results showed that a refractive index mismatch can degrade device performance. On the other hand, results also showed to verify device performance improvement by adding SiO_2 layer under the dipole antenna for small element photodiodes.

The effect of gap size on device performance and resonance phenomena for bulk substrate photo diode and small element photodiode also investigated. We see from the results, for small element photodiodes the resonance shifts largely to higher wavelength [5]. We also see from the results that adding high dielectric constant material shifts the resonance to higher wavelength more for bulk substrate photodiodes compared to thin element photodiodes. This phenomenon can be used to design a photodiode for optical wavelength (1310 nm / 1550 nm).

We have also provided results for nanojet enhance photo-diodes (pn- and MSM-PD). We showed a comparison of nanojet enhanced germanium MSM photodetector with plasmonic enhancement. We see from the results that, nanojet enhanced photodiode can give as much enhancement as plasmonic structures do, which will result in an equal amount of responsivity for each case. Even though the results show that nanojet enhanced photodiode will give less speed than plasmonic enhanced photodiode as plasmonic enhanced photodiode confines energy in a much smaller area, the speed of nanojet enhanced device can be improved by changing the composition of the nanojet sphere.

Finally, we have also shown results comparing the enhancement using plasmonic structure and using nanojet for a bulk Si substrate pn photodiode. We see that there is a large enhancement in intensity compared to plasmonic structure, which can dramatically improve the performance of the photodetector.

Chapter 10

Future Work

The next step in this work is to implement the nanjet enhanced photodetector experimentally is also our next endeavor. As the FDTD simulated results already shows great potential of this device, so implementing it experimentally is a worthwhile next step. We also want to see the improvement in device performance for a device with both plasmonic and nanjet enhanced structure. As nanopillar, nanocone and nanoprism has been implemented for solar cells which has achieved good results, so applying those plasmonic structures is also a consideration. Designing nanojet enhanced photodiode for optical wavelength (1310 nm / 1550 nm) is also our future endeavor as, so far we have implemented it for visible and near-infrared wavelength. As plasmonic enhanced small element photodiode has shown resonance at higher wavelengths, so designing a photodiode for optical wavelength is also our next considerations.

References

[1] A. Taflove and S. C. Hagness, *Computational Electrodynamics: The Finite-Difference Time-Domain Method*, 3rd Ed., Artech House, Norwood, MA, 2005, pp. 21-406.

[2] A. D. Rakic *et al.*, "Optical properties of metallic films for vertical-cavity optoelectronic devices," *Applied Optics*, Vol. 37, No. 22, August 1, 1998.

[3] J. A. Shackleford *et al.*, "Integrated Plasmonic Lens Photodetector," *Appl. Phys. Lett.*, 94, February 2009.

[4] T. Ishi *et al.*, "Si Nano-Photodiode with a Surface Plasmon Antenna," *JSAP Express Letter*, Vol. 44, No. 12, 2005, pp. L364-L366.

[5] L.Tang *et al.*, "C-shaped nanoaperture-enhanced germanium photodetector," *Optics Letters*, Vol. 31, No. 10, May 15, 2006.

[6] L.Tang *et al.*, "Nanometre-scale germanium photdetector enhanced by a near-infrared dipole antenna," *Nature Photonics*, Vol. 2, April 2008.

[7] L. Tang *et al.*, "Plasmonic device in silicon CMOS," *Electronics Letters*, Vol. 45, No. 13, June 18, 2009.

[8] A. Heifetz *et al.*, "Photonic Nanojets," *Journal of Computational and Theoretical Nanoscience*, Vol. 6, No. 9, 2009.

[9] C. Argyropoulos *et al.*, "Study of an optical nanolens with the parallel finite-difference time-domain technique," *Radio Science*, Vol. 46, July, 2011.

[10] P. Muhlschlegel *et al.*, “Resonant Optical Antennas,” *Science*, Vol. 308, June 2005.

[11] H. Fischer and O. J. F. Martin, “Engineering the optical response of plasmonic nanoantennas,” *Optics Express*, Vol. 16, No. 12, June 2008.

[12] Z. Yu *et al.*, “Design of midinfrared photodetectors enhanced by surface plasmons on grating structures,” *Appl. Phys. Lett.*, 89, October 2006.

[13] N. Das *et al.*, “Light absorption enhancement in metal-semiconductor-metal photodetectors using plasmonic nanostructure gratings,” *HONET*, December 2009.

[14] H. Rajagopalan *et al.*, “Investigation of Semiconductor Nanostructures Photovoltaic for Next Generation Solar Cells,” *AP-S/URSI* 2011.

[15] J. Hetterich *et al.*, “Optimized Design of Plasmonic MSM Photodetector,” *IEEE Journal of Quantum Electronics*, Vol. 43, No. 10, October 2007.

[16] J. S. White *et al.*, “ Extraordinary optical absorption through subwavelength slits,” *Optics Letters*, Vol. 34, No. 5, March 1, 2009.